

Time-Lag properties associated with LFQPO in X-ray variability classes of GRS 1915+105: Findings from *AstroSat*

Prajjwal Majumder^{1*}, Broja G. Dutta^{1†}, Anuj Nandi^{2‡}

¹*Department of Physics, Rishi Bankim Chandra College, Naihati, West Bengal 743165, India.*

²*Space Astronomy Group, ISITE Campus, U. R. Rao Satellite Centre, Outer Ring Road, Marathahalli, Bangalore, 560037, India.*

Accepted XXX. Received YYY; in original form ZZZ

ABSTRACT

We present a comprehensive analysis of Low Frequency Quasi-periodic Oscillation (LFQPO) associated time-lags in the persistently variable black hole binary GRS 1915+105 using 441 ks of *AstroSat* observations from March 2016 to March 2019. LFQPO frequency (1.38 – 7.38 Hz) are detected across the θ , β , ρ , and χ classes, with the χ class further subdivided into χ_1 , χ_2 , χ_3 , and χ_4 based on spectro-temporal characteristics. Class transitions occur on timescales of a few hours, appearing either as a simultaneous increase in X-ray count rate and QPO frequency, or vice versa, indicating rapid changes in the accretion flow geometry. The rms_{QPO} increases with QPO frequency up to ~ 3.4 Hz and declines at higher frequencies, a trend similar to *RXTE* observations, where peak occurred at ~ 2 Hz. Spectro-temporal correlations reveal that increasing F_{Comp} drives higher rms_{QPO} and decreases the soft-lag magnitude, while ν_{QPO} and Γ also decline, suggesting that the observed time lag may result from the combined effects of multiple physical mechanisms. The consistent increase of rms_{QPO} with F_{Comp} provides clear evidence that modulated Comptonized photons enhance the rms power (rms_{QPO}). Moreover, the soft-lag (1.59 – 13.49 ms) observed across all QPO frequencies, without the sign reversal at ~ 2 Hz observed in *RXTE* observations, is interpreted within the framework of a dynamical accretion disk model around the black hole.

Key words: accretion, accretion disc – black hole physics – X-rays: binaries – stars: individual: GRS 1915+105

1 INTRODUCTION

Compact objects accrete material from their companion stars either through Roche lobe overflow or by capturing stellar wind. Such systems are typically bright in X-rays (Frank et al. 2002) and are classified as X-ray binaries (XRBs; Seward & Charles 2010). When the compact object is a black hole, these systems are referred to as black hole XRBs (BH-XRBs). Some BH-XRBs show variability in their X-ray flux on timescales ranging from milliseconds to a few days and are known as persistently variable sources, e.g., GRS 1915+105 (Muno et al. 1999a; Belloni et al. 2000; Athulya et al. 2022, and references therein). Studying the time variability properties of these BH-XRB sources is crucial for understanding key black hole characteristics such as spin and mass, as well as the geometry of accretion flows and jet formation (Vadawale et al. 2001a; Reig & Kylafis 2015; Radhika et al. 2016).

The variability properties of BH-XRBs can be understood from time-series analysis of their lightcurves. A sharp rise in frequency-dependent power in the Power Density Spectrum (PDS) is identified as a Quasi-periodic Oscillation (QPO), with frequencies (ν) ranging from ~ 0.1 to 450 Hz. Based on their frequency, QPOs are classified into two categories: (a) low-frequency QPOs (LFQPOs), with $\nu < 40$ Hz, and (b) high-frequency QPOs (HFQPOs), with ν in the range of 40–450 Hz (Remillard & McClintock 2006).

HFQPOs are detected only in a few BH-XRBs (Belloni et al. 2012; Sreehari et al. 2020), whereas LFQPOs are ubiquitous across nearly all systems. Based on their PDS morphology and time-lag properties, LFQPOs are categorized into three types, type-A, type-B, and type-C (Wijnands et al. 1999; Casella et al. 2004, 2005; Nandi et al. 2012, and references therein). Of the three types, type-C QPOs occur most frequently, and observed in both transient and persistent BH systems. Several models have been proposed to explain the origin of LFQPOs. Stella & Vietri (1998); Ingram et al. (2009) proposed the Lense-Thirring precession of the inner accretion disk as the origin of LFQPOs due to the relativistic frame-dragging effect around rotating black holes. Additionally, the jet precession model (Ferreira et al. 2022) proposes that LFQPOs may arise from instabilities at the base of the jet. Such precession changes the jet’s orientation, which in turn modulates the observed X-ray emission, giving rise to LFQPOs. The most promising explanation comes from the two-component advective flow model (Chakrabarti & Titarchuk 1995; Chakrabarti & Manickam 2000; Rao et al. 2000; Vadawale et al. 2001b; Iyer et al. 2015), supported by numerical simulations (Molteni et al. 1994; Garain et al. 2014; Das et al. 2014; Aktar et al. 2018), which attributes LFQPOs to the oscillatory behaviour of the post-shock region in the accretion flow around a black hole. This region acts as a Comptonizing cloud.

GRS 1915+105 has exhibited both LFQPOs and HFQPOs since its discovery in 1992. The LFQPOs of this source have been extensively studied using *RXTE* observations (Chen et al. 1997; Muno et al. 1999a; Markwardt et al. 1999; Reig et al. 2000; Nandi et al. 2001a).

* E-mail: majumderprajjwal@gmail.com

† E-mail: brojadutta@gmail.com

‡ E-mail: anuj@ursc.gov.in

In fact, type-C QPOs are present in the majority of *RXTE* pointing with ~ 620 observations (Zhang et al. 2020). However, type-B QPOs have also been reported by Soleri et al. (2008) during the β and μ classes in *RXTE* data. The rms amplitude of type-C QPOs increases with frequency up to ~ 2.2 Hz and then decreases as the QPO frequency rises further (Yan et al. 2013; Zhang et al. 2020). However, the frequency of type-B QPOs does not show any correlation with their rms amplitude (Soleri et al. 2008). Munro et al. (1999a) studied the spectro-temporal correlations of LFQPOs in GRS 1915+105 and found that the centroid frequency increases with the temperature of the inner disc. They also noted that the power-law component dominates the spectrum when QPOs are present, whereas the disc blackbody component dominates when QPOs are absent. Additionally, Rodriguez et al. (2004) investigated the rms amplitude as a function of energy and concluded that QPOs could originate from the modulation of the Comptonized X-ray flux. Owing to its rich variability and frequent detection of QPOs, GRS 1915+105 provides an excellent opportunity for studying the connection between the evolution of spectral and timing properties such as time-lag behaviour at QPO frequency.

BH-XRBs exhibit complex time-lag behaviour associated with LFQPOs, which remains challenging to interpret as it depends on the relative contributions of various physical processes such as Comptonization, reflection and on the geometry of the system (Dutta & Chakrabarti 2016). Using Monte Carlo simulations considering the two-component advective flow geometry, and incorporating Comptonization, gravitational light bending and reflection, Chatterjee et al. (2017) demonstrated that the time-lag decreases with the shrinking size of the Compton cloud during the rising phase, and increases again during the declining phase. The phase-lag of type-C QPOs strongly depends on inclination and QPO frequency (see van den Eijnden et al. 2017; Choudhury et al. 2025). In case of high inclination sources, phase-lag decreases with QPO frequency while for low inclination sources, phase-lag increases with QPO frequency (Reig et al. 2000; Pahari et al. 2013; van den Eijnden et al. 2017; Zhang et al. 2020). This trend, along with the role of multiple physical mechanisms, has been observationally confirmed in both transient and persistent sources using *RXTE* data (Dutta & Chakrabarti 2016; Dutta et al. 2018; Patra et al. 2019; Chatterjee et al. 2020; Nandi et al. 2021; Debnath et al. 2024; Majumder et al. 2024, 2025b; Sahu et al. 2024; Choudhury et al. 2025).

In GRS 1915+105, the time-lag switches sign from positive to negative at a QPO frequency of ~ 2.2 Hz during the *RXTE* era (Reig et al. 2000; Pahari et al. 2013; Dutta et al. 2018; Zhang et al. 2020). Despite these temporal studies, the correlation between spectral properties and phase/time-lags at LFQPOs have not been extensively studied. However, Majumder et al. (2024) showed through a broadband (0.7–50 keV) spectral study that the Comptonizing medium has a high optical depth ($\tau \sim 6.90 - 12.55$), and the magnitude of the soft-lag associated with HFQPOs increases linearly with increasing τ . This naturally motivates a systematic investigation of correlation between spectral properties and time-lag at LFQPOs, which could provide crucial insights into the accretion geometry and radiative processes in black hole systems.

GRS 1915+105 has also been extensively observed with *AstroSat*, where both LFQPOs and HFQPOs have been detected (Yadav et al. 2016; Rawat et al. 2019; Belloni et al. 2019; Banerjee et al. 2021; Athulya et al. 2022; Athulya & Nandi 2023; Sreehari et al. 2020; Majumder et al. 2022; Harikesh et al. 2025; Majumder et al. 2025a). The first detection of LFQPO was observed during the χ class, with frequencies varying between 2–8 Hz, and detailed time-lag analysis revealed a soft-lag at the corresponding QPO frequency (Yadav et al.

2016). Rawat et al. (2019) further studied the source during χ , IMS, and ρ class observations, reporting strong LFQPOs in the 3–5 Hz range, with soft-lags at the fundamental QPO and hard-lags at the harmonic. Additionally, Banerjee et al. (2021) reported LFQPOs in the 4–5 Hz range during θ class observations.

Athulya et al. (2022) performed the first comprehensive analysis of all *AstroSat* observations (MJD 57705–58648) of GRS 1915+105, identifying six variability classes (χ , ρ , ω , δ , κ , and γ), with LFQPOs detected mainly in the χ and ρ classes. The β class was later reported by Majumder et al. (2022), though without detailed LFQPO analysis. Spectral studies further revealed accretion dynamics during LFQPOs. Misra et al. (2020) found an anti-correlation between LFQPO frequency and the inner disc radius during χ , IMS, and ρ classes. More recently, Belloni et al. (2024) explored the time-lag properties of GRS 1915+105 during χ class observations and concluded that the size of the corona is correlated with the QPO frequency. Despite these important contributions, time-lag studies at LFQPOs with *AstroSat* remain incomplete. In particular, a systematic spectro-temporal investigation of time-lag properties associated with type-C QPOs is still absent in literature. Moreover, no sub-classification of χ class observations has yet been attempted using the rich *AstroSat* datasets.

In this work, we present a comprehensive spectro-temporal study of 441 ks observations of all LFQPOs of GRS 1915+105 using *AstroSat*. Light curves and colour–colour diagrams (CCDs) were generated to identify the variability classes. The χ class observations were further sub-classified into χ_1 , χ_2 , χ_3 , and χ_4 , following the scheme of Belloni et al. (2000). Fourier analysis was then carried out to characterize the LFQPO features and to investigate the associated time-lag properties at the corresponding QPO frequencies. In addition, detailed wide-band spectral analysis was performed to correlate the time-lag properties and spectral parameters.

We organize this paper as follows. In §2, we describe the data reduction procedures for *MAXI*, *BAT*, and *AstroSat*. The methods of timing and spectral analysis are presented in §3. The results and the spectro-temporal correlations are discussed in §4. In §5, we interpret our findings in the context of existing theoretical models. Finally, we summarize our conclusions in §6.

2 OBSERVATION AND DATA REDUCTION

We analyzed the *AstroSat* observations obtained between 4 March 2016 and 22 March 2019, when LFQPOs were detected. However, we excluded the analysis of the observations during the re-brightening period of obscured phase (Athulya & Nandi 2023). The considered observations were compared against the long-term simultaneous flux variations and ‘colour’ diagram from *MAXI/GSC* (2–10 keV) and *Swift/BAT* (15–50 keV), as shown in the lightcurve in Fig. 1. We defined the ‘colour’ as the ratio of *BAT* (15–50 keV) to *MAXI* (2–10 keV) counts/flux, expressed in Crab units. The selected *AstroSat* observations are indicated by coloured vertical lines in the same figure. In this work, we considered a total of 42 observations, with a cumulative exposure time of 441 ks. The details of these observations are provided in Table 1.

2.1 *MAXI* Data Reduction

The Gas Slit Camera (*GSC*) (Mihara et al. 2011), onboard the Monitor of All-sky X-ray Image (*MAXI*) mission, has been continuously monitoring GRS 1915+105 since 11 August 2009. In this

work, we utilize data from the *MAXI/GSC* website¹ to analyze the source’s lightcurve in the 2–10 keV energy range. The *GSC* count rates are converted to Crab units² by dividing count rate by ~ 3.74 photons/s/cm² (see also [Motta et al. 2021](#)).

2.2 BAT Data Reduction

The Burst Alert Telescope (*BAT*), onboard the Neil Gehrels Swift Observatory ([Krimm et al. 2013](#)), has been monitoring the source since 15 February 2005. The long-term *BAT* lightcurve of GRS 1915+105 in the 15–50 keV energy band was downloaded from the *Swift/BAT* website³. The lightcurve was then converted to Crab units, assuming an average Crab count rate of 0.22 counts/s/cm².

2.3 AstroSat Data Reduction

AstroSat ([Agrawal 2006](#); [Singh et al. 2014](#)) is the first multi-wavelength astronomy mission launched by India, in 2015. We utilized observations from the Soft X-ray Telescope (*SXT*) ([Singh et al. 2017](#)) and the Large Area X-ray Proportional Counter (*LAXPC*) ([Yadav et al. 2016](#); [Antia et al. 2017](#)) for spectro-temporal analysis of the source.

The *SXT* ([Singh et al. 2017](#)) observes X-ray sources in the 0.3–8 keV energy range with a timing resolution of 2.3775 s. Due to this limited time resolution, we performed only spectral analysis using the Level-2 *SXT* data available from the *AstroSat* public archive⁴.

For the *LAXPC* ([Yadav et al. 2017](#)), we used Level-1 data from the same archive⁴ for timing and spectral analysis. Timing analysis was performed by processing the Level-1 data into Level-2 using the *LAXPCSOFTWARE* pipeline. The resulting Level-2 data were then used to study the temporal properties of all observations.

Wide-band (0.7–60 keV) spectral analysis was performed for the *AstroSat* observations by combining data from *SXT* (0.7–7 keV) and *LAXPC* (3–60 keV). Due to high count rate in observations AS1 to AS25 (see Table 1), we extracted top-layer single-event *LAXPC20* spectra using *LAXPCSOFTV3.4.3* as suggested by [Antia et al. \(2021\)](#). The corresponding *SXT* spectra were generated considering an annulus region with inner and outer radii of 3′ and 7′, respectively, to minimize pile-up effects caused by high count rates during these observations (see Table 1). For the remaining observations, we used all layers of *LAXPC20*, and the *SXT* spectra were extracted using a circular region with a radius of 12′, appropriate for the relatively lower count rates.

All *SXT* spectra were grouped to have a minimum of 30 counts per bin, while no grouping was applied to the *LAXPC20* spectra. A systematic error of 3% was added to both sets of spectra ([Antia et al. 2021](#)). To account for instrumental feature near the Si and Au edges at 1.8 keV and 2.2 keV ([Singh et al. 2017](#)), respectively, we applied the gain fit (see [Majumder et al. 2024](#), and references therein) command in *XSPEC* version 12.12.0 ([Arnaud 1996](#)).

3 ANALYSIS AND MODELLING

We carried out a detail spectro-temporal analysis of selected archival *AstroSat* observations when LFQPOs were detected. Our aim is to ex-

plore the generic time-lag properties associated with LFQPOs across different phases and variability classes and then to compare the results with those obtained from *RXTE* observations.

3.1 Timing Analysis

3.1.1 Lightcurve and CCD

We generate 1s binned background subtracted lightcurves for the *AstroSat* observations, in the 3–6 keV (band A), 6–15 keV (band B), and 15–60 keV (band C) energy bands by combining *LAXPC10* and *LAXPC20* data ([Sreehari et al. 2020](#)). To plot the CCD, we define soft and hard colours as $HR1=B/A$ and $HR2=C/A$, respectively. The background subtracted and dead-time corrected lightcurve in 3–60 keV and CCD for *AstroSat* observations are shown in Fig. 2. The average count rate, HR1 and HR2 for all observations are tabulated in Table 1.

3.1.2 Power Spectrum and Cross Spectrum Analysis

We performed Fourier analysis using 1 ms binned lightcurves from *AstroSat* observations to generate power density spectra (PDS). The lightcurves were produced by combining data from *LAXPC10* and *LAXPC20* in the 3–60 keV energy band and PDS is generated using the *POWSPEC* tool in *HEASOFT* v6.29c. Each segment consisted of 65,536 bins (i.e., 65,536 s in length), and the resulting PDS were further averaged to obtain the final spectrum. A geometric rebinning factor of 1.02 was applied for the power spectral analysis. The dead-time corrected Poisson noise was then subtracted following [Agrawal et al. \(2018\)](#), and the final PDS was normalized in squared rms units ([Belloni & Hasinger 1990](#)). The PDS are modelled in *XSPEC* V12.12.0 using multiple Lorentzian. The Lorentzian feature with Q-factor ≥ 3 and significance ($\sigma = \frac{Norm}{Norm_{err}}$) ≥ 3 ([Belloni et al. 2012](#); [Sreehari et al. 2019](#)) are classified as QPOs. We further calculated the percentage rms amplitude of the QPO as $100 \times \sqrt{Norm}$ ([van der Klis 1989](#); [Wang et al. 2024](#)).

The time lag is calculated from the argument of the complex cross-spectrum (see [Vaughan & Nowak 1997](#), for details), which is defined as $C(j) = X_1^*(j)X_2(j)$, where $X_1(j)$ and $X_2(j)$ are the Fourier coefficients corresponding to two different energy bands at frequency $\nu(j)$ ([van der Klis et al. 1987](#)). We computed the cross-spectrum between the 6–20 keV and 3–6 keV energy bands using the *LAXPCsoftware*, based on data from *LAXPC10* and *LAXPC20* ([Majumder et al. 2024](#)). The frequency resolution and Nyquist frequency were set to 0.1 Hz and 250 Hz, respectively. The time lag was then averaged over the FWHM of the QPO feature, following the method described by [Reig et al. \(2000\)](#). The resulting power density spectrum (PDS) and time-lag spectrum are shown in Fig. 3, while the centroid frequency, FWHM, fractional rms amplitude, and average time-lag are listed in Table 1.

To ensure a consistent comparison of time lags between *RXTE* and *AstroSat*, we adopted the closest possible reference energy bands. Since the 3–6 keV band could not be used for most *RXTE* observations due to data structure limitations, we selected the lowest available band (2–5 keV) as the reference and computed the time lag for the 5–20 keV band. For the energy-dependent analysis, we divided the *AstroSat* data into seven bands (3–6 keV, 6–9 keV, 9–12 keV, 12–15 keV, 15–18 keV, 18–21 keV and 21–25 keV), calculated the QPO fractional rms (rms_{QPO}) as a function of energy, and derived the average time lag from the cross-spectrum relative to the 3–6 keV band.

¹ <http://maxi.riken.jp/top/lc.html>

² http://maxi.riken.jp/star_data/J0534+220/J0534+220.html

³ <https://swift.gsfc.nasa.gov/results/transients/>

⁴ https://webapps.issdc.gov.in/astro_archive/archive/Home.jsp

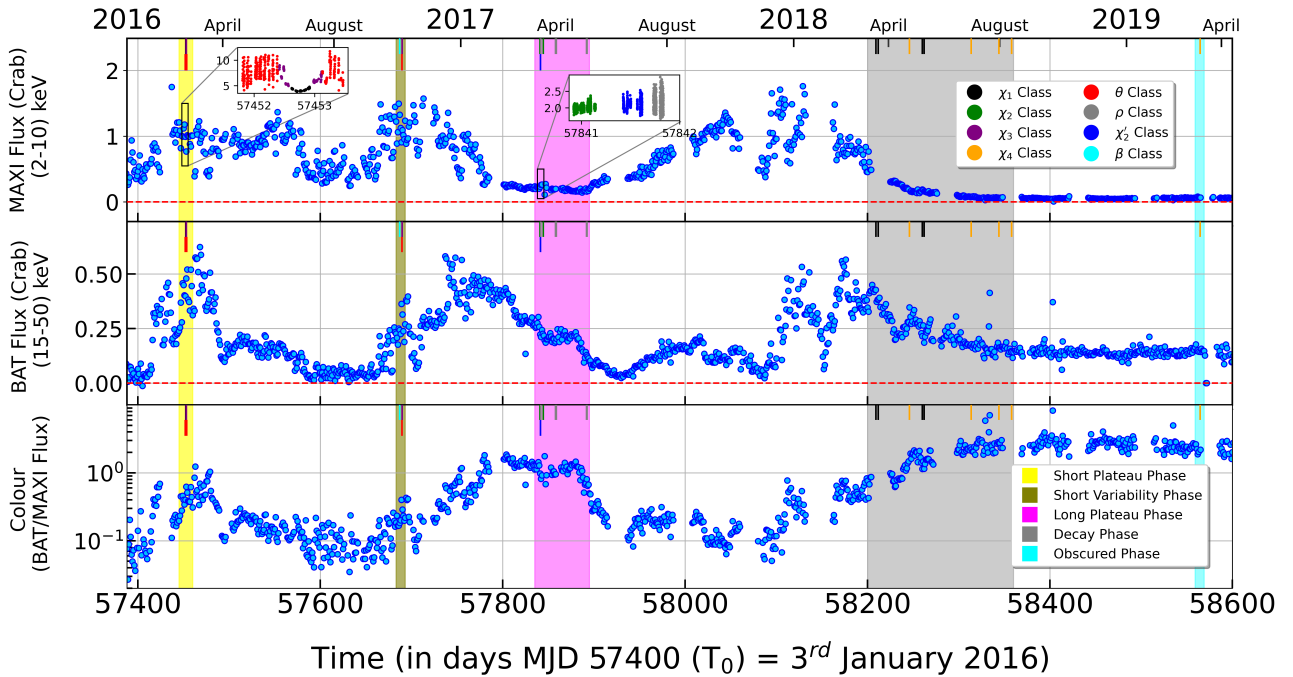


Figure 1. The *MAXI/GSC* (2–10 keV) and *Swift/BAT* (15–50 keV) lightcurves of GRS 1915+105 from January 2016 to April 2019 are plotted in the unit of Crab, shown in the upper and middle panels respectively. The ‘Colour’ in the lower panel is defined as the ratio of *BAT* flux to the *MAXI* flux. The coloured vertical lines represent the considered *AstroSat* observations of different variability classes mentioned in the legend in the upper panel. All observations can be classified as five different phases, shown in the legend in lower panel. See text for details.

3.2 Energy Spectral Analysis

We performed spectral analysis of the *SXT* and *LAXPC20* data (0.7–60 keV) using *XSPEC* v12.12.0 (Arnaud 1996), available as part of *HEASOFT* v6.29c. All spectra were fitted using the model combination $\text{constant} \times \text{TBabs} \times (\text{thcomp} \otimes \text{diskbb})$. The constant component accounts for cross-calibration differences between the two instruments. The *TBabs* model (Wilms et al. 2000) represents Galactic absorption along the line of sight. The *diskbb* component (Mitsuda et al. 1984; Makishima et al. 1986) models the thermal emission from the accretion disk, while the convolution model *thcomp* (Zdziarski et al. 2020) describes the thermal Comptonization of seed photons from the disk that are reprocessed in the corona. In addition, we included an instrumental Xenon edge near ~ 32 keV as required (Antia et al. 2017; Sreehari et al. 2020; Majumder et al. 2022).

The hydrogen column density (N_{H}) was fixed at 6×10^{22} atoms cm^{-2} for most of the observations (Muno et al. 1999b; Sreehari et al. 2020). However, for observations from MJD 58246 onward, N_{H} was left free and was found to lie in the range $2.15 - 5.17 \times 10^{22}$ atoms cm^{-2} (Athulya & Nandi 2023). The best-fit spectral parameters, along with the error in 90% confidence intervals, are presented in Table 2. We also calculated the bolometric flux in the 1–100 keV energy range using the *cflux* model component and expressed it as a percentage of the Eddington luminosity, assuming a black hole mass of $12.4 M_{\odot}$ and a distance of 8.6 kpc (Reid et al. 2014). Furthermore, we calculated the individual contributions of the Comptonized flux and the disk flux to the total flux, which are also listed in Table 2. Finally, the optical depth (τ) of the Comptonizing medium was calculated using the relation given by Zdziarski et al. (1996).

4 RESULTS

In this work, we present a detailed analysis of the energy-dependent fast variability properties of GRS 1915+105 during intervals exhibiting LFQPOs, using *AstroSat* observations. These were correlated with long-term flux measurements from *MAXI* (2–10 keV) and *BAT* (15–50 keV) between January 2016 and April 2019 (see Fig. 1) to study flux variations across energy bands. All LFQPO detections were grouped into five distinct phases, corresponding to different variability classes observed by *AstroSat* as mentioned below.

- (i) Short Plateau Phase (MJD 57451 – 57453)
- (ii) Short Variability Phase (MJD 57688 – 57689)
- (iii) Long Plateau Phase (MJD 57840 – 57892)
- (iv) Decay Phase (MJD 58209 – 58358)
- (v) Obscured Phase (MJD 58564)

These five phases (i) to (v) are highlighted by yellow, olive, magenta, grey, and cyan shaded regions, respectively, in Fig. 1. Interestingly, the ‘colour’ remains nearly constant at ~ 1 throughout all phases except the Short Variability Phase, indicating that the source persistently resides in a harder spectral state. Variability class transitions were observed only during the Short Plateau Phase (MJD 57451 – 57453), Short Variability Phase (MJD 57688 – 57689) and in the initial period of Long Plateau Phase (MJD 57840 – 57892) due to the availability of continuous observations during these intervals. Despite the similar magnitude of ‘colour’, each phase exhibits distinct variability classes and fast variability characteristics of each class.

4.1 Variability Classes during Different Phases

The source was found to be in the θ , β , ρ , and χ variability classes of GRS 1915+105 during the considered observations, consistent with

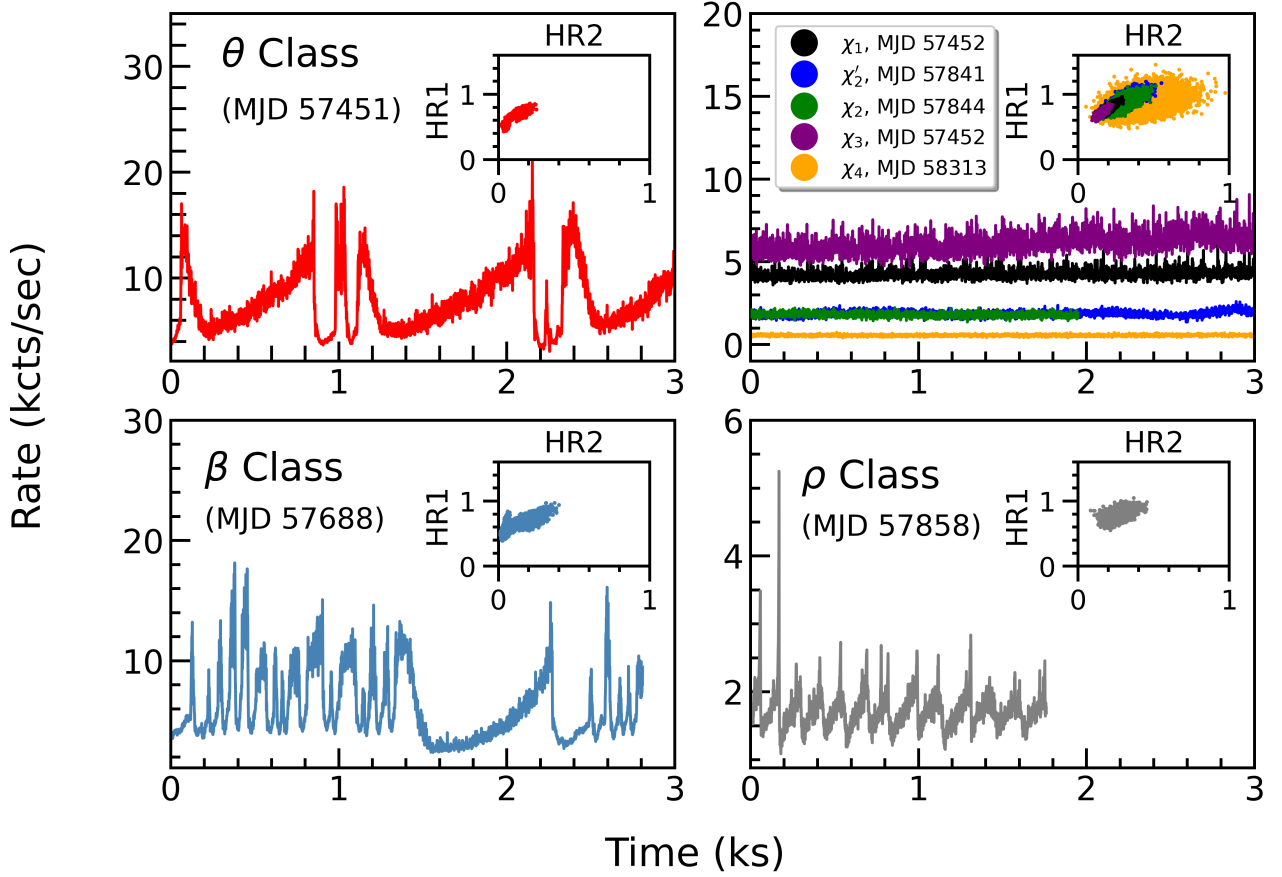


Figure 2. Lightcurve and CCD of variability classes (θ , χ , β , ρ) of the source GRS 1915+105 during LFQPO observations using *AstroSat*. The background subtracted and dead-time corrected 1s binned *LAXPC* lightcurves are plotted in the 3–60 keV energy range with CCD (top-right inset). The sub-classifications of χ class is shown in the top-right panel. See text for detail.

classifications reported by [Yadav et al. \(2016\)](#), [Rawat et al. \(2019\)](#), [Athulya et al. \(2022\)](#), and [Majumder et al. \(2022\)](#). Lightcurves in the 3–60 keV energy band for each variability class are shown in Fig. 2, with the corresponding CCD displayed in the top-right corner of each panel. The variability class and the respective MJD are mentioned in the top-left corner of each panel. The lightcurve during θ class, exhibits a characteristic ‘M’ shaped intervals (see top-left panel in Fig. 2) with typical durations of a few hundred seconds. Furthermore, the β class displays highly irregular and complex variability signatures (see bottom-left panel in Fig. 2) followed by a prolonged low-count intervals. In contrast, the ρ class shows heartbeat-like variability (see also [Athulya et al. 2022](#)), which is shown in the bottom-right panel in Fig. 2. The ‘harder’ variability class χ typically shows relatively low variability in count rates and a CCD dominated by high-energy photons, with HR2 values extending to the higher value (see top-right panel of Fig. 2). Following [Belloni et al. \(2000\)](#) and [Sreehari et al. \(2020\)](#), we further sub-classify the χ class into χ_1 , χ_2 , χ_3 , and χ_4 based on average count rate and hardness ratios (HR1 and HR2) as shown in the top-right panel of Fig. 2. Among these, χ_3 shows the highest count rate (8445 – 5487 cts/s) with the lowest hardness, while χ_1 exhibits lower count rates (1065 – 4731 cts/s) with relatively higher hardness. χ_2 shows hardness greater than both χ_3 and χ_1 , with count rates of 1779 – 1853 cts/s. The χ_4 sub-class exhibits the maximum hardness, with HR2 extending further to the higher value, and the lowest count rates (380 – 1282 cts/s). The variability

classes and the class transitions observed during different phases are presented as follows.

- **Short Plateau Phase (SPP):** The source exhibits rapid variability over a ~ 1.5 day period (MJD 57451 – 57453), characterized by a short dip-like feature in the lightcurve persisting for ~ 15 hours. The count rate drops from 8336 to 3998 cts/s within a day, followed by a rise to 8059 cts/s in the next day. Interestingly, the hardness ratios exhibit an opposite trend where it increases initially and decreases further (see Table 1). During this phase, the source undergoes a transition through the $\theta \rightarrow \chi \rightarrow \theta$ classes ([Yadav et al. 2016](#); [Majumder et al. 2022](#); [Belloni et al. 2024](#)). Moreover, the study of hardness ratio during χ class indicates that the source goes through a transition $\chi_3 \rightarrow \chi_1 \rightarrow \chi_3$. The lightcurve and CCD for χ_1 and χ_3 in MJD 57452 is shown in the top-right panel of Fig. 2. Hence, the class transition during SPP is observed to be: $\theta \rightarrow \chi_3 \rightarrow \chi_1 \rightarrow \chi_3 \rightarrow \theta$ (see Table 1).

- **Short Variability Phase (SVP):** During this phase, the *MAXI* light curve shows a variable feature, while the *BAT* flux rises sharply from 0.25 to 0.37 Crab in the 15 – 50 keV band (see middle panel of Fig. 1). Simultaneously, the source ‘colour’ increases from ~ 0.1 to ~ 0.5 (see lower panel), indicating a hardening for short interval. During this phase, β class is observed, as first reported by [Majumder et al. \(2022\)](#) (see bottom-left panel of Fig. 2). However, our detailed analysis reveals that the source exhibits θ class afterwards, following by a short interval of χ class which can be sub-classified as χ_3

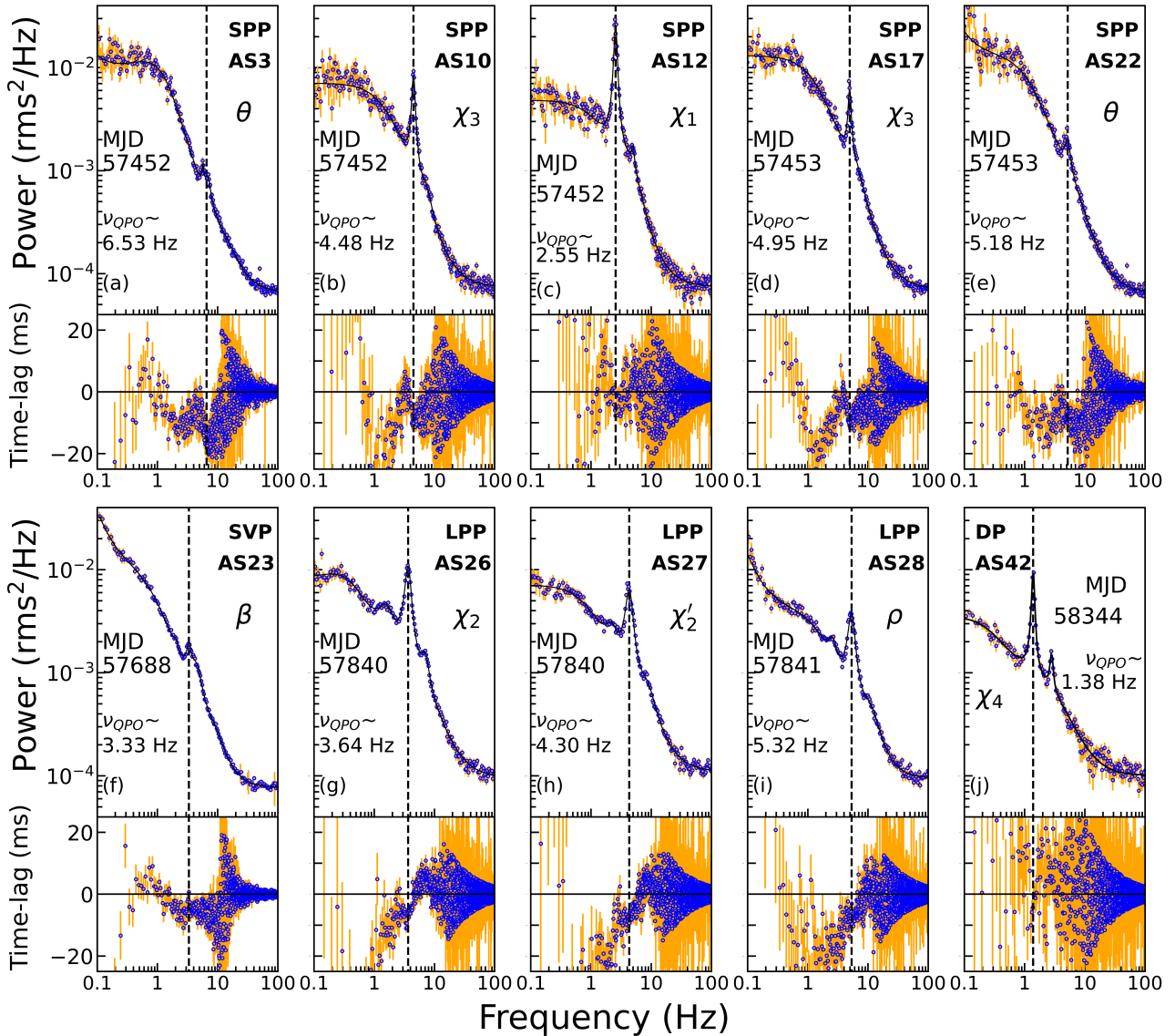


Figure 3. The broadband PDS (3–60 keV) and time-lag spectra (6–20 keV w.r.t 3–6 keV) corresponding to different variability classes of *AstroSat* observations. The MJD of each observation and the QPO frequency are mentioned in each panel. The dashed vertical black line corresponds to the QPO frequency. See text for details.

based on hardness ratio (see Table 1). Hence, the source undergoes a transition from $\beta \rightarrow \theta \rightarrow \chi_3$ during this phase. The average count rate rises from 6158 to 10,664 cts/s, accompanied by an increase in the average hardness ratio (see Table 1). Notably, the count rate of the χ_3 class in this observation is significantly higher than that observed during the Short Plateau Phase.

- **Long Plateau Phase (LPP):** During this phase (MJD 57840 – 57892), the *MAXI* flux remained nearly constant at approximately 0.2 Crab for 52 days, while the *BAT* flux gradually declined from about 0.2 to 0.09 Crab (see Fig. 1). The source count rate varied between 1451 and 1929 counts/s, with an overall decrease in both HR1 and HR2. Between MJD 57840 and 57841 (AS26–AS28), the source was reported to exhibit a transition from $\chi \rightarrow IMS \rightarrow \rho$ class, where *IMS* represents an intermediate transitional state between χ and ρ (Rawat et al. 2019). The sub-classification indicates the aforementioned χ to be χ_2 . Additionally, the *IMS* class identified in earlier studies, exhibits long-term, large-amplitude, irregular variab-

ility only on timescales of a few thousand seconds. This behaviour is observed only in the soft X-ray band (3–5 keV) and exhibits strong similarities in CCD with the χ_2 class (see the inset in top-right panel in Fig. 2). However, it exhibits a clear modulation in the lightcurve (see Rawat et al. 2019, for details). Therefore, despite the lack of significant spectral differences, the subtle timing variations provide sufficient support to conclude that the *IMS* is a subset of χ_2 , which we designate as the χ_2' variability class. Hence, within one day (MJD 57840 – 57841) the source exhibits a class transition of $\chi_2 \rightarrow \chi_2' \rightarrow \theta$. Beyond MJD 57841, the source exhibited χ_2 and ρ variability class during this entire phase.

- **Decay Phase (DP):** During this phase, beginning around MJD 58209, both *MAXI* flux (2–10 keV) and *BAT* flux (15–50 keV) start to decline, and this decay continues for ~ 150 days (see Fig. 1). The average source count rate drops from 2929 cts/s to 397 cts/s, while the hardness ratios gradually increase (see Table 1 for details). This trend is also observed in the colour variation of the source shown

Table 1. Observation details of the source GRS 1915+105 observed by *AstroSat* during March 2016 to March 2019. In the table, Mission (ID), ObsID and MJD start are mentioned. The detected r_{det} count rates for all observations with hardness ratios and variability classes are also tabulated. Furthermore, we tabulated the temporal parameters of the Fourier analysis, that is, centroid frequency (ν_{QPO}) and FWHM of the QPO feature, along with the percentage rms amplitude in 3 – 60 keV band. The time lag of 6 – 20 keV w.r.t 3 – 6 keV at ν_{QPO} is tabulated in milliseconds. See text for details.

Mission (ID)	ObsID	MJD	r_{det} (cts/s)	HR1 (B/A)*	HR2 (C/A)*	Class	ν_{QPO} (Hz)	FWHM (Hz)	rms _{QPO} (%)	Time-lag (ms)
Short Plateau Phase (SPP)										
AS1	T01_030T01_9000000358	57451.81	8336	0.68	0.12	θ	5.32 ^{+0.12} _{-0.09}	1.82 ^{+0.58} _{-0.38}	4.18 ± 0.60	-8.80 ± 0.45
AS2	T01_030T01_9000000358	57451.89	7741	0.67	0.12	θ	5.24 ^{+0.21} _{-0.21}	1.03 ^{+0.32} _{-0.27}	3.21 ± 0.62	-8.98 ± 0.49
AS3	T01_030T01_9000000358	57452.04	9856	0.69	0.12	θ	6.53 ^{+0.11} _{-0.11}	2.34 ^{+0.37} _{-0.32}	3.85 ± 0.26	-13.49 ± 0.46
AS4	T01_030T01_9000000358	57451.98	8937	0.67	0.12	θ	5.95 ^{+0.12} _{-0.10}	2.74 ^{+0.44} _{-0.35}	3.58 ± 0.28	-10.81 ± 0.28
AS5	T01_030T01_9000000358	57451.98	9487	0.68	0.12	θ	6.33 ^{+0.12} _{-0.12}	2.82 ^{+0.36} _{-0.31}	3.35 ± 0.15	-12.22 ± 0.21
AS6	T01_030T01_9000000358	57452.26	9862	0.68	0.12	θ	5.45 ^{+0.15} _{-0.13}	1.15 ^{+0.36} _{-0.35}	3.11 ± 0.48	-8.46 ± 0.71
AS7	T01_030T01_9000000358	57452.33	9666	0.67	0.12	θ	5.50 ^{+0.29} _{-0.10}	0.55 ^{+0.66} _{-0.25}	1.93 ± 1.04	-10.56 ± 1.14
AS8	T01_030T01_9000000358	57452.41	8445	0.68	0.13	χ_3	5.61 ^{+0.07} _{-0.07}	0.45 ^{+0.16} _{-0.14}	4.18 ± 0.64	-11.51 ± 0.87
AS9	T01_030T01_9000000358	57452.48	8049	0.68	0.13	χ_3	4.56 ^{+0.04} _{-0.04}	0.25 ^{+0.10} _{-0.09}	2.68 ± 0.36	-6.54 ± 1.19
AS10	T01_030T01_9000000358	57452.55	5487	0.68	0.14	χ_3	4.48 ^{+0.02} _{-0.02}	0.61 ^{+0.06} _{-0.05}	8.47 ± 0.21	-8.76 ± 0.50
AS11	T01_030T01_9000000358	57452.62	4549	0.71	0.16	χ_1	3.55 ^{+0.02} _{-0.01}	0.48 ^{+0.04} _{-0.02}	10.65 ± 0.25	-7.00 ± 0.53
AS12	T01_030T01_9000000358	57452.68	3998	0.78	0.19	χ_1	2.55 ^{+0.01} _{-0.01}	0.33 ^{+0.02} _{-0.02}	11.31 ± 0.31	-4.42 ± 0.66
AS13	T01_030T01_9000000358	57452.75	4027	0.77	0.18	χ_1	2.79 ^{+0.01} _{-0.01}	0.36 ^{+0.02} _{-0.02}	11.23 ± 0.26	-6.46 ± 0.56
AS14	T01_030T01_9000000358	57452.82	4286	0.74	0.17	χ_1	3.25 ^{+0.02} _{-0.02}	0.49 ^{+0.04} _{-0.03}	11.01 ± 0.24	-5.69 ± 0.43
AS15	T01_030T01_9000000358	57452.90	4731	0.71	0.15	χ_1	3.85 ^{+0.02} _{-0.02}	0.59 ^{+0.05} _{-0.04}	11.24 ± 0.31	-6.56 ± 0.54
AS16	T01_030T01_9000000358	57452.98	6181	0.69	0.14	χ_3	4.81 ^{+0.02} _{-0.02}	0.65 ^{+0.06} _{-0.06}	7.46 ± 0.27	-9.48 ± 0.30
AS17	T01_030T01_9000000358	57453.06	6606	0.69	0.14	χ_3	4.95 ^{+0.02} _{-0.02}	0.59 ^{+0.06} _{-0.06}	6.69 ± 0.30	-10.08 ± 0.41
AS18	T01_030T01_9000000358	57453.13	7589	0.69	0.13	θ	5.69 ^{+0.08} _{-0.08}	1.65 ^{+0.22} _{-0.21}	5.07 ± 0.30	-9.54 ± 0.33
AS19	T01_030T01_9000000358	57453.21	8351	0.69	0.13	θ	4.93 ^{+0.05} _{-0.05}	1.02 ^{+0.12} _{-0.12}	5.54 ± 0.27	-9.07 ± 0.42
AS20	T01_030T01_9000000358	57453.28	9632	0.69	0.13	θ	5.72 ^{+0.11} _{-0.13}	0.77 ^{+0.23} _{-0.19}	2.77 ± 0.36	-9.93 ± 0.64
AS21	T01_030T01_9000000358	57453.35	9996	0.68	0.12	θ	6.55 ^{+0.17} _{-0.14}	2.48 ^{+0.36} _{-0.41}	3.55 ± 0.28	-12.32 ± 0.66
AS22	T01_030T01_9000000358	57453.42	8059	0.69	0.13	θ	5.18 ^{+0.08} _{-0.07}	1.31 ^{+0.43} _{-0.22}	4.44 ± 0.68	-7.52 ± 0.60
Short Variability Phase (SVP)										
AS23	G06_033T01_9000000760	57688.73	6158	0.62	0.09	β	3.33 ^{+0.06} _{-0.06}	0.61 ^{+0.30} _{-0.32}	2.80 ± 0.54	-4.42 ± 0.68
AS24	G06_033T01_9000000760	57689.54	8142	0.65	0.11	θ	5.74 ^{+0.10} _{-0.10}	3.15 ^{+0.25} _{-0.24}	5.37 ± 0.19	-5.60 ± 0.23
AS25	G06_033T01_9000000760	57689.83	10664	0.67	0.11	χ_3	7.38 ^{+0.06} _{-0.06}	1.32 ^{+0.18} _{-0.15}	3.37 ± 0.15	-11.50 ± 0.63
Long Plateau Phase (LPP)										
AS26	G06_033T01_9000001116	57840.92	1779	1.00	0.37	χ_2	3.64 ^{+0.01} _{-0.01}	0.87 ^{+0.03} _{-0.04}	11.26 ± 0.22	-6.80 ± 0.32
AS27	G06_033T01_9000001116	57841.38	1856	0.91	0.31	χ_2	4.30 ^{+0.02} _{-0.02}	1.30 ^{+0.07} _{-0.08}	10.49 ± 0.21	-7.35 ± 0.34
AS28	G06_033T01_9000001116	57841.72	1929	0.80	0.24	ρ	5.32 ^{+0.02} _{-0.02}	1.50 ^{+0.07} _{-0.06}	8.59 ± 0.15	-7.38 ± 0.31
AS29	G07_046T01_9000001124	57844.49	1853	0.85	0.28	χ_2	4.00 ^{+0.02} _{-0.02}	0.78 ^{+0.08} _{-0.08}	9.87 ± 0.47	-6.51 ± 0.32
AS30	G07_046T01_9000001162	57857.92	1737	0.74	0.23	ρ	4.84 ^{+0.02} _{-0.01}	0.86 ^{+0.06} _{-0.04}	8.06 ± 0.27	-6.93 ± 0.28
AS31	G07_028T01_9000001166	57858.82	1719	0.77	0.26	ρ	4.49 ^{+0.03} _{-0.03}	0.55 ^{+0.07} _{-0.08}	8.92 ± 0.79	-7.53 ± 0.39
AS32	G07_028T01_9000001232	57891.82	1451	0.70	0.21	ρ	4.89 ^{+0.02} _{-0.02}	0.79 ^{+0.06} _{-0.06}	8.05 ± 0.43	-6.09 ± 0.48
AS33	G07_046T01_9000001236	57892.50	1483	0.64	0.20	ρ	5.71 ^{+0.01} _{-0.01}	1.67 ^{+0.05} _{-0.05}	5.99 ± 0.07	-6.05 ± 0.34
Decay Phase (DP)										
AS34	A04_180T01_9000002000	58209.13	2929	0.73	0.21	χ_1	3.29 ^{+0.01} _{-0.01}	0.88 ^{+0.03} _{-0.04}	11.92 ± 0.17	-7.32 ± 0.18
AS35	G08_028T01_9000002006	58211.76	2429	0.69	0.21	χ_1	3.63 ^{+0.01} _{-0.01}	0.91 ^{+0.04} _{-0.04}	10.68 ± 0.14	-6.63 ± 0.18
AS36	G08_028T01_9000002080	58246.00	1282	0.87	0.45	χ_4	2.41 ^{+0.01} _{-0.01}	0.38 ^{+0.02} _{-0.02}	8.17 ± 0.12	-2.87 ± 0.44
AS37	G08_078T01_9000002110	58260.00	1112	0.75	0.25	χ_1	3.93 ^{+0.01} _{-0.01}	0.77 ^{+0.03} _{-0.03}	9.77 ± 0.10	-2.65 ± 0.20
AS38	G08_028T01_9000002112	58262.00	1065	0.75	0.26	χ_1	3.31 ^{+0.01} _{-0.01}	0.65 ^{+0.03} _{-0.03}	9.75 ± 0.15	-5.05 ± 0.30
AS39	G08_028T01_9000002220	58313.57	559	0.86	0.41	χ_4	1.93 ^{+0.01} _{-0.01}	0.21 ^{+0.01} _{-0.01}	5.97 ± 0.08	-2.12 ± 0.63
AS40	G08_028T01_9000002306	58344.43	414	0.89	0.47	χ_4	1.38 ^{+0.00} _{-0.00}	0.15 ^{+0.01} _{-0.01}	4.68 ± 0.11	-2.90 ± 1.78
AS41	G08_028T01_9000002334	58358.00	397	0.85	0.44	χ_4	1.83 ^{+0.00} _{-0.01}	0.17 ^{+0.01} _{-0.01}	4.56 ± 0.11	-1.71 ± 1.42
Obscured Phase (OP)										
AS42	A05_173T01_9000002812	58564.67	380	0.83	0.48	χ_4	2.39 ^{+0.01} _{-0.01}	0.17 ^{+0.01} _{-0.01}	3.89 ± 0.10	-1.59 ± 1.06

* For *AstroSat/LAXPC* observations, A, B and C bands are defined as 3 – 6 keV, 6 – 15 keV and 15 – 60 keV respectively. See [Sreehari et al. \(2020\)](#) for details.

in the bottom panel of Fig. 1. The source remains in the χ class throughout this phase, which we further sub-classify into χ_1 , χ_2 , and χ_4 variability classes. Interestingly, the χ_1 class observations during this period exhibit lower count rates compared to those in the Short Plateau Phase, while maintaining similar hardness ratios.

• **Obscured Phase (OP):** In this phase, the *MAXI* flux (2 – 10 keV) reaches its minimum, while the *BAT* flux (15 – 50 keV) remains nearly constant at ~ 0.15 Crab, leading to the maximum observed ‘colour’ of the source. Analysis of the light curve and CCD confirms that the source corresponds to the χ_4 variability class (see Fig. 2 and Table 1).

4.2 Timing Features in Different Phases

The Fast Fourier analysis of all observations reveal the presence of QPOs with centroid frequencies (ν_{QPO}) ranging from 1.38 to 7.38 Hz and corresponding percentage rms amplitudes (rms_{QPO}) between 1.93% and 11.92% (see Table 1). Distinct variability characteristics associated with ν_{QPO} are observed across the five identified phases. During the SPP, ν_{QPO} exhibits rapid fluctuations, initially decreasing from 5.32 Hz to 2.55 Hz as the count rate declines, and then rising to 6.55 Hz as the count rate increases again (see panels (a) to (e) in Fig. 3). In contrast, the rms_{QPO} follows an opposite trend, increasing from 4.18% to 11.31% as the count rate decreases, and then dropping to 3.55% with the subsequent increase in the count rate.

Interestingly, the QPOs observed during the SVP are quite broad

Table 2. Model parameters of the observations fitted with `constant×TBabs×(thcomp*diskbb)`. The Comptonized flux (F_{Comp}), Disc flux (F_{Disc}) and bolometric luminosity in the unit of Eddington luminosity (L_{Edd}) are calculated in the energy range 1 – 100 keV. All errors are calculated with 90% confidence range. See text for details.

Mission (ID) [†]	Class	Γ	kT_e (keV)	f_{cov}	kT_{in} (keV)	χ^2/dof	$F_{\text{Comp}}(\%)$	$F_{\text{Disc}}(\%)$	$L_{\text{Edd}}(\%)$	τ
Short Plateau Phase (SPP)										
AS1	θ	2.55 ^{+0.03} _{-0.03}	20.00*	0.49 ^{+0.03} _{-0.03}	1.40 ^{+0.04} _{-0.04}	510.64/528	30.41 ± 2.34	69.59 ± 4.06	34.73	2.12 ± 0.04
AS2	θ	2.57 ^{+0.09} _{-0.07}	19.02 ^{+7.94} _{-3.73}	0.52 ^{+0.11} _{-0.07}	1.40 ^{+0.04} _{-0.05}	605.08/551	30.99 ± 1.45	69.01 ± 2.49	29.00	2.17 ± 0.32
AS3	θ	2.63 ^{+0.08} _{-0.08}	18.81 ^{+7.54} _{-3.79}	0.61 ^{+0.14} _{-0.09}	1.33 ^{+0.07} _{-0.08}	333.27/347	33.68 ± 4.17	66.32 ± 6.26	27.19	2.11 ± 0.32
AS5	θ	2.62 ^{+0.09} _{-0.06}	17.91 ^{+3.34} _{-2.50}	0.58 ^{+0.09} _{-0.07}	1.35 ^{+0.07} _{-0.04}	571.01/536	32.49 ± 1.95	67.51 ± 3.02	26.95	2.20 ± 0.23
AS6	θ	2.49 ^{+0.09} _{-0.09}	13.02 ^{+2.99} _{-1.85}	0.43 ^{+0.07} _{-0.06}	1.48 ^{+0.05} _{-0.06}	595.36/557	28.47 ± 1.34	71.53 ± 2.58	22.83	2.96 ± 0.32
AS7	θ	2.51 ^{+0.09} _{-0.09}	13.52 ^{+3.26} _{-2.04}	0.46 ^{+0.08} _{-0.07}	1.43 ^{+0.06} _{-0.06}	206.19/210	30.02 ± 6.14	69.98 ± 11.07	31.80	2.85 ± 0.33
AS8	χ_3	2.51 ^{+0.09} _{-0.09}	15.05 ^{+4.90} _{-2.68}	0.48 ^{+0.09} _{-0.07}	1.46 ^{+0.05} _{-0.05}	570.87/479	30.85 ± 3.82	69.15 ± 6.52	41.70	2.65 ± 0.35
AS9	χ_3	2.57 ^{+0.12} _{-0.11}	19.88 ^{+2.39} _{-5.96}	0.57 ^{+0.12} _{-0.11}	1.38 ^{+0.06} _{-0.06}	516.23/472	33.21 ± 2.70	66.79 ± 4.28	30.97	2.11 ± 0.47
AS10	χ_3	2.51 ^{+0.02} _{-0.02}	19.76*	0.58 ^{+0.05} _{-0.04}	1.23 ^{+0.04} _{-0.04}	456.87/461	36.88 ± 2.36	63.12 ± 3.16	23.91	2.19 ± 0.03
AS11	χ_1	2.54 ^{+0.07} _{-0.07}	27.80 ^{+34.77} _{-9.09}	0.76 ^{+0.21} _{-0.14}	1.06 ^{+0.05} _{-0.06}	463.35/437	43.54 ± 2.61	56.46 ± 2.52	20.11	1.68 ± 0.41
AS12	χ_1	2.44 ^{+0.07} _{-0.08}	23.55 ^{+7.11} _{-7.77}	0.79 ^P _{-0.16}	1.07 ^{+0.07} _{-0.09}	544.82/479	48.90 ± 3.59	51.10 ± 2.75	30.69	2.03 ± 0.49
AS13	χ_1	2.52 ^{+0.02} _{-0.07}	25.98 ^{+8.80} _{-7.92}	0.94 ^P _{-0.23}	0.84 ^{+0.11} _{-0.07}	563.31/485	54.01 ± 3.97	45.99 ± 2.48	32.41	1.79 ± 0.40
AS14	χ_1	2.52 ^{+0.02} _{-0.02}	20.92 ^{+3.75} _{-1.94}	0.87*	0.84 ^{+0.03} _{-0.03}	613.97/543	52.18 ± 3.83	47.82 ± 2.58	34.96	2.09 ± 0.20
AS15	χ_1	2.32 ^{+0.07} _{-0.07}	10.96 ^{+1.98} _{-1.38}	0.47 ^{+0.07} _{-0.06}	1.27 ^{+0.04} _{-0.04}	539.31/511	37.07 ± 2.85	62.93 ± 3.67	33.20	3.67 ± 0.34
AS16	χ_3	2.43 ^{+0.06} _{-0.06}	13.06 ^{+2.29} _{-1.59}	0.50 ^{+0.07} _{-0.05}	1.32 ^{+0.03} _{-0.04}	635.18/532	35.10 ± 1.65	64.90 ± 2.34	25.58	3.06 ± 0.27
AS17	χ_3	2.53 ^{+0.08} _{-0.08}	18.45 ^{+7.15} _{-3.65}	0.56 ^{+0.11} _{-0.08}	1.41 ^{+0.05} _{-0.05}	409.34/339	33.87 ± 4.77	66.13 ± 7.15	35.34	2.27 ± 0.33
AS18	θ	2.50 ^{+0.07} _{-0.08}	14.57 ^{+3.11} _{-2.04}	0.54 ^{+0.08} _{-0.07}	1.30 ^{+0.05} _{-0.05}	538.45/537	34.88 ± 1.05	65.12 ± 1.46	18.33	2.72 ± 0.28
AS19	θ	2.46 ^{+0.08} _{-0.08}	12.87 ^{+2.10} _{-1.66}	0.46 ^{+0.07} _{-0.06}	1.43 ^{+0.05} _{-0.06}	529.33/515	31.40 ± 0.94	68.60 ± 1.53	14.58	3.03 ± 0.30
AS20	θ	2.52 ^{+0.08} _{-0.08}	13.70 ^{+3.26} _{-1.96}	0.49 ^{+0.09} _{-0.06}	1.39 ^{+0.06} _{-0.07}	528.17/548	31.76 ± 1.49	68.24 ± 2.46	21.51	2.81 ± 0.30
AS21	θ	2.57 ^{+0.09} _{-0.09}	14.73 ^{+4.43} _{-2.54}	0.50 ^{+0.10} _{-0.07}	1.43 ^{+0.07} _{-0.07}	296.87/297	30.27 ± 5.16	69.73 ± 9.09	35.63	2.59 ± 0.33
AS22	θ	2.48 ^{+0.08} _{-0.07}	14.54 ^{+3.81} _{-2.28}	0.48 ^{+0.08} _{-0.06}	1.39 ^{+0.04} _{-0.04}	505.02/470	32.08 ± 3.01	67.92 ± 4.90	31.50	2.76 ± 0.32
Short Variability Phase (SVP)										
AS23	β	2.39 ^{+0.17} _{-0.17}	18.14 ^{+12.07} _{-4.46}	0.18 ^{+0.06} _{-0.04}	2.10 ^{+0.05} _{-0.05}	705.00/651	14.50 ± 0.25	85.50 ± 1.21	13.74	2.51 ± 0.50
AS24	θ	2.42 ^{+0.08} _{-0.08}	12.20 ^{+1.85} _{-1.38}	0.35 ^{+0.05} _{-0.04}	1.55 ^{+0.05} _{-0.05}	739.80/668	26.12 ± 0.78	73.88 ± 1.65	31.55	3.21 ± 0.28
AS25	χ_3	2.72 ^{+0.10} _{-0.09}	23.82 ^{+18.01} _{-6.58}	0.58 ^{+0.16} _{-0.10}	1.39 ^{+0.06} _{-0.06}	618.38/551	29.41 ± 1.88	70.59 ± 3.53	33.59	1.69 ± 0.35
Long Plateau Phase (LPP)										
AS26	χ_2	2.04 ^{+0.06} _{-0.06}	29.19 ^{+25.66} _{-7.81}	0.49 ^{+0.16} _{-0.08}	1.19 ^{+0.04} _{-0.06}	653.75/550	51.75 ± 0.84	48.25 ± 0.62	16.19	2.34 ± 0.45
AS27	χ_2'	2.15 ^{+0.03} _{-0.03}	29.00*	0.56 ^{+0.08} _{-0.07}	1.18 ^{+0.05} _{-0.06}	591.47/537	50.34 ± 1.51	49.66 ± 1.11	16.28	2.15 ± 0.05
AS28	ρ	2.15 ^{+0.05} _{-0.04}	29.26*	0.44 ^{+0.09} _{-0.06}	1.32 ^{+0.05} _{-0.06}	627.90/576	42.53 ± 0.74	57.47 ± 0.81	17.01	2.14 ± 0.08
AS29	χ_2	1.97 ^{+0.05} _{-0.05}	15.44 ^{+2.68} _{-1.94}	0.32 ^{+0.04} _{-0.03}	1.31 ^{+0.04} _{-0.03}	621.91/554	43.06 ± 0.75	56.94 ± 0.81	15.90	3.79 ± 0.34
AS30	ρ	2.04 ^{+0.06} _{-0.05}	25.23 ^{+16.55} _{-6.06}	0.28 ^{+0.06} _{-0.03}	1.29 ^{+0.03} _{-0.02}	596.06/633	37.38 ± 0.65	62.62 ± 0.89	12.08	2.59 ± 0.44
AS31	ρ	1.99 ^{+0.04} _{-0.04}	21.76 ^{+6.26} _{-3.87}	0.29 ^{+0.03} _{-0.03}	1.31 ^{+0.02} _{-0.02}	621.51/558	39.91 ± 0.69	60.09 ± 0.85	12.89	2.98 ± 0.37
AS32	ρ	1.90 ^{+0.06} _{-0.05}	15.94 ^{+3.12} _{-2.62}	0.21 ^{+0.03} _{-0.02}	1.36 ^{+0.03} _{-0.02}	572.53/561	35.45 ± 0.61	64.55 ± 0.91	10.70	3.95 ± 0.46
AS33	ρ	1.87 ^{+0.05} _{-0.05}	19.30 ^{+7.24} _{-3.66}	0.16 ^{+0.02} _{-0.02}	1.39 ^{+0.02} _{-0.02}	654.02/633	31.09 ± 0.54	68.91 ± 0.97	10.90	3.58 ± 0.47
Decay Phase (DP)										
AS34	χ_1	2.02 ^{+0.05} _{-0.05}	16.91 ^{+3.13} _{-2.67}	0.39 ^{+0.05} _{-0.04}	1.38 ^{+0.02} _{-0.02}	716.49/650	44.87 ± 0.78	55.13 ± 0.78	28.05	3.44 ± 0.31
AS35	χ_1	2.01 ^{+0.05} _{-0.05}	15.86 ^{+2.67} _{-1.78}	0.36 ^{+0.04} _{-0.04}	1.36 ^{+0.03} _{-0.03}	722.41/642	43.54 ± 0.75	56.46 ± 0.80	23.61	3.61 ± 0.30
AS36	χ_4	1.68 ^{+0.04} _{-0.05}	11.70 ^{+0.94} _{-0.81}	0.32 ^{+0.03} _{-0.03}	1.65 ^{+0.06} _{-0.06}	703.30/630	52.17 ± 0.77	47.83 ± 0.52	11.18	5.89 ± 0.35
AS37	χ_1	1.89 ^{+0.05} _{-0.05}	26.80 ^{+19.10} _{-6.52}	0.40 ^{+0.08} _{-0.05}	1.43 ^{+0.04} _{-0.04}	686.07/652	52.22 ± 0.75	47.78 ± 0.50	11.19	2.83 ± 0.48
AS38	χ_1	1.87 ^{+0.05} _{-0.05}	22.47 ^{+9.64} _{-4.33}	0.37 ^{+0.06} _{-0.05}	1.41 ^{+0.05} _{-0.05}	670.46/619	51.54 ± 0.76	48.46 ± 0.52	10.62	3.24 ± 0.44
AS39	χ_4	1.64 ^{+0.04} _{-0.04}	21.25 ^{+3.33} _{-3.93}	0.44 ^{+0.07} _{-0.07}	1.86 ^{+0.08} _{-0.08}	764.32/618	63.42 ± 0.91	36.58 ± 0.37	6.63	4.26 ± 0.53
AS40	χ_4	1.71 ^{+0.07} _{-0.07}	16.39 ^{+3.67} _{-2.25}	0.64 ^{+0.15} _{-0.11}	2.26 ^{+0.25} _{-0.26}	635.21/574	64.29 ± 0.92	35.71 ± 0.36	5.20	4.64 ± 0.52
AS41	χ_4	1.59 ^{+0.05} _{-0.05}	13.69 ^{+1.89} _{-1.36}	0.35 ^{+0.04} _{-0.04}	1.73 ^{+0.09} _{-0.09}	590.05/533	60.12 ± 0.86	39.88 ± 0.41	4.77	5.92 ± 0.50
Obscured Phase (OP)										
AS42	χ_4	1.59 ^{+0.02} _{-0.02}	14.16 ^{+1.61} _{-1.44}	0.37 ^{+0.05} _{-0.04}	1.77 ^{+0.08} _{-0.08}	704.44/573	60.82 ± 0.25	39.18 ± 0.16	4.38	5.81 ± 0.38

* Frozen parameter

p Parameter pegged at higher limit.

† The spectral analysis of AS4 is not performed due to the unavailability of Level 2 *SXT* products.

(see panel (f) in Fig. 3 and Table 1), with a Q-factor as low as 1.83. The ν_{QPO} increases steadily from 3.33 Hz to 7.38 Hz, while the rms_{QPO} varies between 2.80% and 5.37% (see Table 1). The associated time-lag is soft, ranging between ~ 1 –2 ms. During the LPP, the ν_{QPO} remains nearly constant at ~ 4 –5 Hz (see panels (g)–(i) in Fig. 3), with rms_{QPO} in the range ~ 5.99 –11.26% and a soft-lag of ~ 6.5 ms. In the DP, the QPO frequency decreases to as low as 1.38 Hz (see panel (j) in Fig. 3), with an rms amplitude of

4.68% and associated with a soft-lag of 2.90 ms. Finally, in the OP, the QPO is detected at 2.39 Hz with an rms amplitude of 3.89% and a soft-lag of 1.59 ms. Details of the timing properties are tabulated in Table 1.

Apart from this, we find that different variability classes exhibit distinct ranges of QPO centroid frequencies (ν_{QPO}). The QPO frequency of χ_4 class observations lie in the range 1.38 – 2.41 Hz. Whereas, χ_1 , χ_2 and β class observations show QPO frequency in

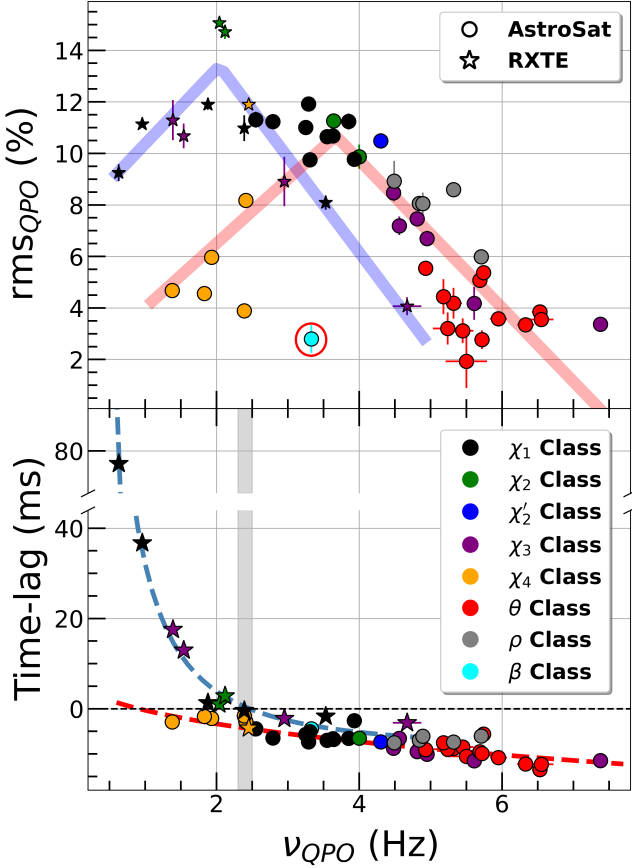


Figure 4. Variation of percentage rms amplitude (rms_{QPO}) and time-lag as a function of the centroid frequency (ν_{QPO}) of the LFQPO. The star and circle represent *RXTE* and *AstroSat* observations respectively. The filled colours correspond to different variability classes shown in the legend. See text for details.

the range 2.55 – 4.30 Hz. However, the χ_2' , χ_3 , ρ and θ class observations lie in an overlapping range of 4.30 – 6.55 Hz.

The broadband (3 – 60 keV) PDS and time-lag spectrum in the frequency domain 0.1 – 100 Hz are shown in Fig. 3 for different phases. We found soft-lag for all observations for all values of ν_{QPO} and the magnitude of soft-lag lies in the range 1.59–13.49 ms. The soft-lag during χ_4 class is observed to be in range of 1.59 – 2.90 ms, which is the minimum. During χ_1 , χ_2 and β classes, the soft-lag lies in the range 2.65 – 7.32 ms. However, the soft-lag during χ_2' , χ_3 , ρ and θ class observations lies in an overlapping range of 6.05 – 13.49 ms. Surprisingly, our analysis shows that the time-lag associated with $\nu_{\text{QPO}} < 2.2$ Hz exhibits a soft-lag (see panel (j) in Fig. 3), in contrast to the hard-lag previously reported at lower ν_{QPO} using *RXTE* observations (Zhang et al. 2020). To verify this result, we rechecked the time-lag analysis of the *AstroSat* data using *GHATS* v3.2.0⁵, and obtained consistent findings.

To investigate the long-term evolution of the QPO properties, we analyzed *RXTE* observations from MJD 50278 to 53214. A clear correlation between ν_{QPO} and rms_{QPO} is observed, as shown in the upper panel of Fig. 4. The star and circle markers represent *RXTE* and *AstroSat* data, respectively, with different variability classes indicated by the colours in the legend. For *AstroSat* observations, rms_{QPO}

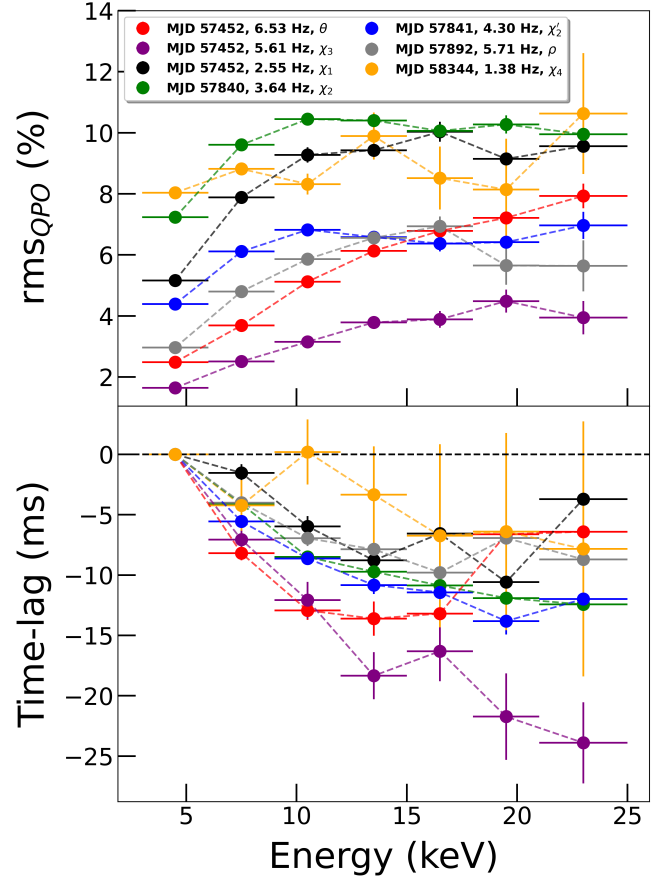


Figure 5. Energy dependent percentage rms amplitude (rms_{QPO}) and time-lag at LFQPO using *AstroSat* shown in the upper and lower panel respectively. Different colours correspond to different observations. The MJD, QPO frequency and variability class are shown in the legend. See text for details.

initially increases with ν_{QPO} and then decreases at higher frequencies. A similar trend is also seen in the *RXTE* data, consistent with the results reported by Zhang et al. (2020). However, in case of *AstroSat* observations we find an exception for the β class (AS23), where it do not follow the similar trend as other observations (marked in red circle; see upper panel in Fig. 4). We fitted the data points of rms_{QPO} as a function of ν_{QPO} , excluding the β class observation for *AstroSat* with broken linear function as follows.

$$\text{rms}_{\text{QPO}}[\text{RXTE}] = \begin{cases} +2.91 \times \nu_{\text{QPO}} + 7.45 & ; \nu_{\text{QPO}} \leq 2.04 \\ -3.69 \times \nu_{\text{QPO}} + 20.92 & ; \nu_{\text{QPO}} \geq 2.04 \end{cases} \quad (1)$$

$$\text{rms}_{\text{QPO}}[\text{AstroSat}] = \begin{cases} +4.21 \times \nu_{\text{QPO}} - 2.81 & ; \nu_{\text{QPO}} \leq 3.42 \\ -3.22 \times \nu_{\text{QPO}} + 22.61 & ; \nu_{\text{QPO}} \geq 3.42 \end{cases} \quad (2)$$

The model fitted broken linear function for both *RXTE* (blue) and *AstroSat* (red) is shown in the upper panel of Fig. 4. Interestingly, the source does not follow the same trend during *AstroSat* observations as during *RXTE* observations. The break frequency (ν_{QPO} , where rms_{QPO} is maximum) during *RXTE* era was found to be at 2.04 Hz, which agrees with the results obtained by Zhang et al. (2020). However, during *AstroSat* observations the break frequency is found to be 3.42 Hz. We find maximum rms_{QPO} for χ_1 and χ_2 variability classes for both *RXTE* and *AstroSat* observations.

A correlation is also obtained between the average time-lag (δt)

⁵ http://astrosat-ssc.iucaa.in/uploads/ghats_home.html

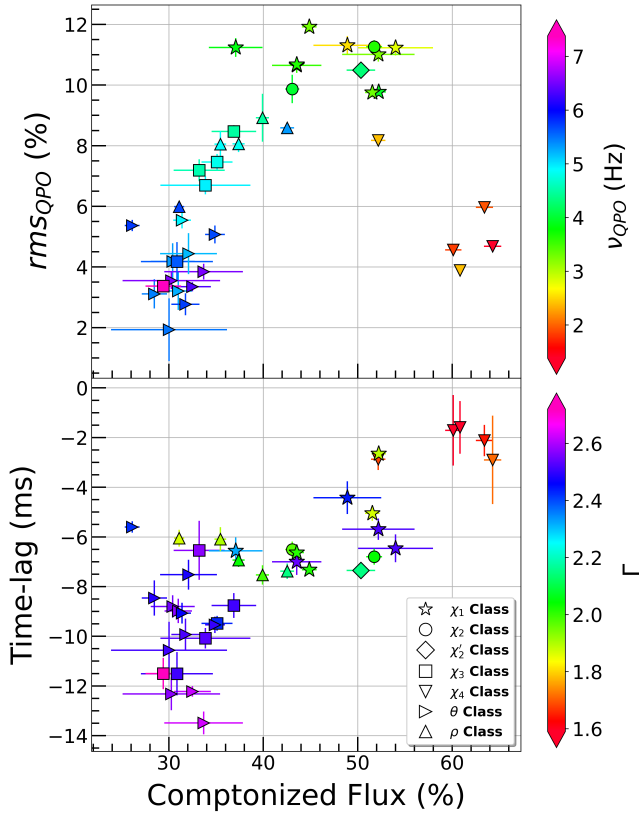


Figure 6. The correlation between rms_{QPO} and Comptonized flux percentage is plotted in the upper panel along with the ν_{QPO} as a colour-bar. In lower panel, the variation of time-lag as a function of Comptonized flux is shown along with spectral index (Γ) as colour-bar. Different markers represents different variability class which is shown in the legend. See text for details.

and ν_{QPO} , which is shown in the lower panel of Fig. 4. The circle and star represent the *AstroSat* and *RXTE* observations respectively and the filled colours represent different variability classes. For *RXTE* observations, the time-lag increases as the ν_{QPO} decreases and switches its sign from soft-lag to hard-lag at ~ 2.2 Hz (Reig et al. 2000; Dutta et al. 2018; Zhang et al. 2020). However, in our analysis of *AstroSat* observations, the time-lag increases as ν_{QPO} decreases, but it does not switch sign and remains negative even for $\nu_{\text{QPO}} \leq 2.2$ Hz. We further fitted the data points of time-lag (δt) as a function of ν_{QPO} with a power-law function as follows,

$$\delta t[\text{RXTE}] = +41.61 \times (\nu_{\text{QPO}})^{-1.63} - 9.47 \quad (3)$$

$$\delta t[\text{AstroSat}] = -6.29 \times (\nu_{\text{QPO}})^{+0.53} + 5.71 \quad (4)$$

The fitted powerlaw for *RXTE* and *AstroSat* is shown as blue and red dashed line respectively in the lower panel of Fig. 4. The switching frequency (ν_{QPO} , where $\delta t = 0$; $\nu_{\text{QPO}|\delta t=0}$) for *RXTE* observation is ~ 2.2 Hz whereas, for *AstroSat* observation the $\nu_{\text{QPO}|\delta t=0} = 0.85$ Hz. It is also important to note that for *RXTE* observation χ_1 and χ_3 classes were exhibited hard-lag, whereas for *AstroSat* observation both classes show soft-lag. In *AstroSat* era, only χ_4 exhibits minimum soft-lag of 1.6 ms whereas, θ class exhibits maximum soft-lag ~ 13.5 ms and both these classes show distinct lag feature. Additionally both of these classes are distinctly separated by region in the time-lag and ν_{QPO} correlation diagram (see lower panel in Fig. 4) whereas, other classes remained in overlapping region.

It is noteworthy that the β class observation do not lie in the correlation between rms_{QPO} and ν_{QPO} (marked in red circle; see upper panel in Fig. 4) and it also exhibits soft-lag at the corresponding ν_{QPO} (see Table 1). Soleri et al. (2008) reported similar behaviour for type-B QPOs in the β and μ classes, where type-B QPOs do not exhibit the rms_{QPO} and ν_{QPO} correlation as seen in type-C QPOs, and moreover type-B QPOs are associated with soft-lags. This suggests that the QPO observed in the β class during *AstroSat* corresponds to a type-B QPO, while those in other variability classes are consistent with type-C QPOs.

4.3 Energy Dependent Variability Study

The energy-dependent variability analysis depicts how the rms_{QPO} evolves with energy across different variability classes, as shown in the upper panel of Fig. 5. The observation dates (MJD), corresponding variability classes, and ν_{QPO} are indicated in the legend. For all variability classes, the rms_{QPO} increases with energy, indicating a strong energy dependence. Notably, the energy dependent rms_{QPO} variations differ distinctly among classes up to ~ 15 keV. Beyond this energy, the rms_{QPO} variation exhibits a nearly flat trend. The rms_{QPO} is generally lower for higher ν_{QPO} values and in the χ_1 and χ_4 classes, while it is higher for lower ν_{QPO} values, particularly in the χ_3 class. These distinct energy dependent rms_{QPO} trends suggest a strong correlation between QPO properties and the underlying physical mechanisms responsible for QPO generation in the hard spectral states.

The energy-dependent time-lag measurements relative to the 3–6 keV band for all variability classes observed by *AstroSat* are presented in the lower panel of Fig. 5. For all observations, we consistently detect soft-lags, where higher-energy photons arriving earlier than the 3–6 keV photons, regardless of the QPO frequency (ν_{QPO}) or variability class. In all cases, the magnitude of the soft-lag increases with energy. Notably, the slope of soft-lag variation differs across variability classes and QPO frequencies. Specifically, the soft-lag is highest in the χ_3 class and at higher ν_{QPO} values, while it is comparatively lower in the χ_4 class and at lower ν_{QPO} values. This behaviour clearly indicates that photons in higher energy bands experience larger soft lags, thereby ruling out band-selection effects as the origin of the observed soft lag.

4.4 Results of Spectral Analysis

In this work, we carried out a detailed spectral analysis to explore the connection between the energy spectra and time-lag properties of GRS 1915+105 during observations exhibiting LFQPOs. Such LFQPOs are generally associated with the hard and hard-intermediate spectral states of BH-XRBs. For the considered observations, the photon index vary between $\Gamma = 1.59 - 2.63$, while the electron temperature (kT_e) ranges from 10.96 to 29.26 keV. The covering fraction is found to vary between $f_{\text{cov}} = 0.16 - 0.94$, and the bolometric luminosity lies in the range 4.38–41.70% of the Eddington luminosity (see Table 2). These spectral characteristics, specifically, the relatively low photon index, higher electron temperature, and lower bolometric luminosity are consistent with the source being in the low-hard or hard-intermediate state during the LFQPO intervals (Titarchuk & Fiorito 2004). Different spectral characteristics are observed across different phases of evolution of LFQPO. During the SPP, the photon index (Γ) remains relatively constant, ranging between 2.32 and 2.63. As the source undergoes the transition $\theta \rightarrow \chi_3 \rightarrow \chi_1$, the percentage of Comptonized flux (F_{Comp}) increases from 30.41% to 54.01%. Interestingly, during the subsequent reverse transition $\chi_3 \rightarrow \theta$, F_{Comp}

decreases again to 30.27% (see Table 2). This evolution is consistent with the hardness ratio reported in Table 1, which exhibits a similar trend (see §4.1).

During the SVP, the percentage disc flux (F_{Disc}) is found to be relatively high, ranging from 70.59% to 85.50%. However, during the rapid transition $\beta \rightarrow \theta \rightarrow \chi_3$, the Comptonized flux (F_{Comp}) increases from 14.50% to 29.41%, accompanied by an increase in the covering fraction (f_{cov}) from 0.18 to 0.58. This indicates a clear spectral hardening of the source within a single day (see Table 2).

In the LPP, the spectral parameters remain relatively stable. The photon index (Γ) is observed in the range 1.87–2.15, which is noticeably lower than during the SVP, indicating a comparatively harder spectrum. During this phase, F_{Comp} gradually decreases from 51.75% to 31.09%, a trend also reflected in the hardness ratio (see Table 1).

Conversely, during the DP, F_{Comp} gradually increases from 44.87% to 60.12%, while Γ decreases from 2.02 to 1.59, suggesting that the source is evolving toward a harder spectral state. The lowest bolometric luminosity ($L_{\text{Edd}} \sim 4.4\%$) is observed during the OP, when the source reaches its minimum count rate but still exhibits LFQPOs, implying that the mechanism responsible for QPOs do not depend on the luminosity of the source.

4.5 Spectro-temporal Correlation Study

A correlation between the spectral (F_{Comp} and Γ) and temporal parameters (rms_{QPO} , ν_{QPO} and time-lag) of the source is established to account for the observed time-lag behaviour. The variations in spectral parameters during phases exhibiting LFQPOs are systematically compared with the corresponding timing parameters, as presented in Tables 1 and 2. We excluded the β class observation from this correlation study, as it exhibits type-B LFQPOs (see §4.2). The upper panel of Fig. 6 presents the correlation between rms_{QPO} and the percentage Comptonized flux (F_{Comp}), with the LFQPO centroid frequency (ν_{QPO}) shown as a colour-bar. Different variability classes are represented by distinct markers as indicated in the legend. The rms_{QPO} increases sharply with F_{Comp} up to $\sim 12\%$, except for four χ_4 class observations during the decaying (DP) and obscured (OP) phases, when the total source count rate drops to $\sim 300\text{--}600$ counts/s, indicating a dependence of rms_{QPO} on the source flux. The maximum rms_{QPO} , reaching at $\sim 45\%$ F_{Comp} , is observed mainly during the χ_1 , χ_2 , and χ_2' observations. A clear anti-correlation is also observed between F_{Comp} and ν_{QPO} , with ν_{QPO} decreasing as F_{Comp} increases. The highest F_{Comp} values are found in the χ_4 class, where ν_{QPO} reaches its minimum and the source flux declines to a few percent of the bolometric luminosity ($\sim 4.38\%$ L_{Edd}), consistent with this class representing the extreme hard state of the source.

In the lower panel of Fig. 6, we find clear evidence that the magnitude of the soft-lag decreases with F_{Comp} as the source moves toward harder spectral states, indicated by the decreasing photon index Γ shown in the colour bar. Thus, a strong spectro-temporal correlation is observed, as F_{Comp} increases, the QPO fractional rms (rms_{QPO}) increases and the soft-lag magnitude decreases, while both ν_{QPO} and the photon index Γ decrease. This suggests that as the source transitions toward a harder spectral state, the corona expands (leading to a decline in ν_{QPO}), Comptonization (F_{Comp}) becomes more dominant, and the time-lag increases, though it remains negative. We also find a similar correlation between time-lag and hardness ratio, as hardness primarily traces the relative contribution of hard to soft photons and thus serves as a proxy for the efficiency of the Comptonization process. The near-linear increase in time-lag with rising F_{Comp} across all *AstroSat* observations indicates that the lag arises from the combined effects of multiple physical processes, with Comptonization consist-

ently contributing a positive component (Dutta & Chakrabarti 2016). These correlations further suggest that variations in the Comptonized flux play a key role in driving the evolution of temporal features observed in GRS 1915+105.

5 DISCUSSION

In this work, we have carried out a comprehensive study of variability classes of GRS 1915+105, using *AstroSat* observations spanning March 2016 to March 2019. Our primary aim was to investigate the class transitions and correlating the spectro-temporal properties in order to explain the observed time-lag behaviour, and to compare these results with those obtained from earlier *RXTE* observations.

5.1 Class Transitions: Probing Time Scale of Accretion Flow

Based on the long-term *MAXI/GSC* and *BAT* light curves (see Fig. 1), all LFQPO detections are grouped into five distinct phases: a Short Plateau Phase (SPP); lasting ~ 15 hours in the *LAXPC* light curve (see inset, upper panel of Fig. 1), a Short Variability Phase (SVP); characterized by small variability features over ~ 50 days, a Long Plateau Phase (LPP); a relatively stable period with minimal variation in the *MAXI* light curve, a Decay Phase (DP); during which both *MAXI* and *BAT* flux decrease gradually, and finally, an Obscured Phase (OP); where the source reaches its lowest *MAXI* flux. Across these phases, LFQPOs are detected in eight variability classes: θ , χ_1 , χ_2 , χ_2' , χ_3 , χ_4 , β , and ρ , with their light curves and CCDs shown in Fig. 2.

During the SPP, the source undergoes a rapid transition, $\theta \rightarrow \chi_3 \rightarrow \chi_1 \rightarrow \chi_3 \rightarrow \theta$, within nearly two days where, the inter-class transition is observed within ~ 2 hours (see Table 1). At the beginning of this phase, the count rate, QPO frequency (ν_{QPO}), and disc flux (F_{Disc}) decrease, while the rms amplitude (rms_{QPO}) and Comptonized flux (F_{Comp}) increase, indicating a recession of the inner disc edge and an expansion of the Comptonizing region within few hours (see Table 1 and 2). The enhanced F_{Comp} leads to a higher rms_{QPO} (Chakrabarti & Manickam 2000), consistent with the accretion dynamics predicted by the two-component advective flow (TCAF) paradigm (Chakrabarti & Titarchuk 1995; Molteni et al. 1996; Rao et al. 2000; Nandi et al. 2001b; Das et al. 2014). Subsequently, the source returns to its initial variability class (θ), with all spectral and timing parameters recovering their previous values, indicating that the accretion geometry is restored to its original configuration within a few hours. This behaviour points to a highly variable accretion flow that evolves on timescales of just a few hours, after which the system reverts to its initial variability class. Such rapid variations are consistent with previous findings, where Yadav et al. (2016) reported a correlation between QPO frequency and bolometric flux, and also, Belloni et al. (2024) showed that the variation of Comptonizing region as the QPO frequency increases or decreases (see Chakrabarti & Manickam 2000; Chakrabarti et al. 2005; Dutta et al. 2018; Karpouzas et al. 2021; Athulya et al. 2022; Belloni et al. 2024).

During the SVP, the source undergoes a rapid class transition $\beta \rightarrow \theta \rightarrow \chi_3$ within a day. The QPOs are broad, and *AstroSat* detects a type-B QPO in the β class for the first time. The concurrent rise in disc flux (F_{Disc}) to its highest level further supports the association of type-B QPOs with enhanced disc emission during this variability class (Choudhury et al. 2025, and references therein). As the source progresses through $\theta \rightarrow \chi_3$, the QPO transitions from type-B to type-C, accompanied by increases in both ν_{QPO} and count rate within a few

hours, indicating a similar geometrical variation of the Comptonizing region as observed during the SPP.

During the LPP, the source exhibits a class transition $\chi_2 \rightarrow \chi'_2 \rightarrow \rho$ again within a day where the canonical class transition occur within ~ 7 hours. While [Rawat et al. \(2019\)](#) classified the interval between χ and ρ as an Intermediate State (IMS), our analysis find this state closely resembles with χ_2 , and we therefore classify it as χ'_2 . During this short transition, the count rate, ν_{QPO} , and F_{Disc} increase, while the rms_{QPO} and F_{Comp} decrease, reflecting a variation in accretion geometry similar to that observed in the SPP and SVP (see [Table 1](#) and [2](#)). Similarly, [Misra et al. \(2020\)](#) reported that the QPO frequency increases as the inner disc radius contracts inward. Beyond this short transition, the source remains in the χ_2 and ρ classes, showing relatively minor variations in count rate, ν_{QPO} , and rms_{QPO} , while F_{Comp} gradually decreases, in agreement with previous findings for the χ class ([Dutta et al. 2018](#); [Karpouzias et al. 2021](#)).

During DP, the source is observed in the χ_1 and χ_4 classes (see [Fig. 3](#)). The count rate, ν_{QPO} , rms_{QPO} , and F_{Disc} gradually decrease, accompanied by a reduction in bolometric luminosity (see [Table 1](#) and [2](#)). In contrast, the source hardness and F_{Comp} increase over time, consistent with [Athulya et al. \(2022\)](#). This hardening is also evident in the colour variation shown in the lower panel of [Fig. 1](#). The lowest count rate and bolometric flux ($4.38\% L_{\text{Edd}}$) are observed during the χ_4 variability class in the subsequent Obscured Phase (OP).

Therefore, we find similar variations in count rate, ν_{QPO} , F_{Disc} , rms_{QPO} , and F_{Comp} during rapid class transitions across the SPP, SVP, and LPP phases. Interestingly, the variability class transition occurs on timescales of just a few hours and are accompanied by an increase in count rate with rising QPO frequency or the opposite trend. The key feature is the significant change in count rate between pre- and post-transition phases of variability classes, occurring over remarkably short timescales. Similar rapid variability class transitions have also been frequently observed in *RXTE* data, where such short timescales suggest the disappearance and reformation of the inner accretion disc ([Belloni et al. 1997a,b](#)). The observed increase in count rate implies a rise in the accretion rate, driving the corresponding increase in QPO frequency, while the transition duration reflects the infall timescale ([Nandi et al. 2001a](#); [Chakrabarti et al. 2005](#); [Iyer et al. 2015](#); [Das et al. 2021](#); [Athulya et al. 2022](#)). However, interpreting these class transitions with viscous timescales would require unrealistically low viscosity in a Keplerian disc ([Belloni et al. 1997b](#)). [Chakrabarti et al. \(2005\)](#), using *IXAE* and *RXTE* data, showed that such rapid transitions cannot occur on viscous timescales; instead, a fraction of the accretion flow must be nearly free-falling, i.e., sub-Keplerian in nature. Furthermore, [Athulya et al. \(2022\)](#) proposed that these transitions could occur on thermal–viscous timescales, driven by variations in the sub-Keplerian flow caused by radiation-pressure–induced instabilities in the inner disc near the compact object, thereby triggering the rapid variability class transitions.

5.2 Sub-Classification of χ class: Dynamical Hard state

In *AstroSat* observations, GRS 1915+105 is predominantly found in the χ class (23 of 42 observations), exhibiting characteristics consistent with earlier *RXTE* results ([Belloni et al. 2000](#); [Rao et al. 2000](#); [Huppenkothen et al. 2017](#)). We further sub-classify these observations into χ_1 , χ_2 , χ_3 , and χ_4 based on count rate, hardness, power spectra and time-lag spectra while [Belloni et al. \(2000\)](#) classified them solely on the basis of hardness. As shown in the upper-right panel of [Fig. 2](#), the different χ sub-classes display distinct variations in count rate and hardness (see inset of the same panel). The hardness

is lowest for χ_1 and χ_3 , and highest for χ_4 , while the average count rate is highest in χ_3 and lowest in χ_4 .

Distinct features are also evident in the PDS and energy spectra across the χ sub-classes. The χ_3 class shows a strong QPO frequency without harmonics ([Fig. 3](#), panels b and d), while χ_1 exhibits a weak harmonic without any sub-harmonic during the SPP (panel c), but shows both harmonic and sub-harmonic during the DP. Similarly, the χ_2 class displays QPOs with both harmonic and sub-harmonic features (panel g). However, the PDS of χ'_2 shows a subtle difference, where the sub-harmonic and harmonic humps seen in the χ_2 , are weaker in the PDS of χ'_2 (see [Fig. 3](#), panels g and h). In contrast, χ_4 consistently exhibits a sharp low-frequency QPO accompanied by a strong harmonic (panel j). These distinctions highlight class-dependent signatures of QPOs, harmonics, and sub-harmonics in the frequency–power domain. Time-lag analysis clearly shows that χ_4 class observations exhibit the minimum soft-lag, χ_3 class displays the maximum soft-lag, while intermediate lag values are observed for the χ_1 and χ_2 classes. These differences in soft-lag correspond to variations in spectral properties, where the Comptonized flux (F_{Comp}) is lowest in χ_3 (average $\sim 33\%$), moderate in χ_1 and χ_2 (average $\sim 47\%$), and highest in χ_4 (average $\sim 60\%$).

The χ sub-classes also exhibit distinct radio properties, as evident from *RXTE* observations. [Vadawale et al. \(2003\)](#) modeled χ_{RQ} (radio-quiet; χ_2 , χ_4) spectra using a multi-colour disc along with Comptonized component, whereas χ_{RL} (radio-loud; χ_1 , χ_3) spectra required an additional power-law component. However in our analysis, the spectra of all χ sub-classes are modelled similarly, without incorporating the additional power-law component. [Yadav et al. \(2016\)](#) classified χ class observations during the Short Plateau Phase (SPP) as radio-quiet, whereas our results suggest them to be radio-loud, however, simultaneous radio data are unavailable, making definitive classification uncertain on the basis of radio emission. Finally, a connection between time-lag and radio flux has been reported by [Pahari et al. \(2013\)](#) using *RXTE* data, where χ_{RL} (plateau states) show hard-lags and χ_{RQ} exhibit soft-lags. In contrast, our *AstroSat* observations show soft-lags across all χ sub-classes. The cause of this variation remains unclear, likely due to the lack of simultaneous radio coverage.

5.3 Possible Accretion Disc Configuration

The systematic variation between spectral and timing properties across variability classes and transition phases provides strong evidence for a coherent underlying accretion disc dynamics that governs the behaviour of this persistently variable source during the LFQPOs observed with *AstroSat*. We find that class transitions consistently occur within a few hours, invariably appearing as a significant increase in the X-ray photon count rate accompanied by a rise in QPO frequency. This rapid variation suggests that changes in the accretion rate cannot occur on viscous timescales; instead, a substantial fraction of the accreting matter must be nearly less viscous in nature and follow free-fall timescales, i.e., sub-Keplerian in nature. Such fast transitions further support the presence of a two-component advective flow, a scenario already established for this source ([Chakrabarti & Titarchuk 1995](#); [Chakrabarti & Nandi 2000](#); [Nandi et al. 2001b](#); [Chakrabarti et al. 2002](#); [Dutta et al. 2018](#)). Within the TCAF paradigm ([Chakrabarti & Titarchuk 1995](#)), each QPO frequency corresponds to a specific location of the shock front, defining the size of the oscillating Comptonizing region i.e., corona. Variations in QPO frequency during class transitions therefore indicate gradual geometrical variations in the corona, may driven by fluctuations in the sub-Keplerian accretion rate. These rapid variations likely govern the

observed spectro-temporal evolution and trigger the variability class transitions (Chakrabarti & Nandi 2000; Nandi et al. 2001a; Chakrabarti et al. 2002, 2004, 2005, 2009; Dutta & Chakrabarti 2010). A similar variation in QPO frequency observed in GRS 1915+105 during the *RXTE* observations has been attributed to geometric changes in the Comptonizing region or corona (Zhang et al. 2020; Karpouzas et al. 2021; García et al. 2022; Méndez et al. 2022; Belloni et al. 2024).

The variations in spectro-temporal parameters during variability classes exhibiting LFQPOs confirm that rms_{QPO} increases sharply with F_{Comp} up to $\sim 12\%$, except for four χ_4 class observations when the source flux drops dramatically to $\sim 4.38\%$ of L_{Edd} . This behaviour provides clear evidence supporting the predictions of the TCAF paradigm, where oscillations of the corona enhance the modulation of Comptonized photons, thereby increasing the rms power (rms_{QPO}) in the frequency domain (Chakrabarti & Manickam 2000). Furthermore, the highest F_{Comp} values observed in the χ_4 class, despite the lowest source flux during the hardest spectral state (lowest value of Γ), indicate an enhanced Comptonization rate, consistent with the expected geometry of the TCAF model.

The lower panel of Fig. 6 shows that as F_{Comp} increases, magnitude of the soft-lag decreases while the photon index Γ also decreases, indicating a transition toward a harder spectral state. This establishes a strong spectro-temporal interdependence, with increasing F_{Comp} , the QPO fractional rms (rms_{QPO}) increases and the magnitude of the soft-lag decreases, while both ν_{QPO} and Γ decrease. These correlations suggest that as the source hardens, the corona expands (leading to a reduction in ν_{QPO}), Comptonization becomes more dominant, and the magnitude of the soft-lag decreases, although net time-lag remains negative. This behaviour suggests that the observed time-lag results from the combined effects of multiple physical processes, which include Comptonization, reflection, outflows/jets, and the geometry of the accretion disc (Cui 1999; Nowak et al. 1999; Poutanen & Fabian 1999; Kara et al. 2013; Dutta & Chakrabarti 2016; Chatterjee et al. 2017, 2020; Nandi et al. 2021, 2024). Among these, Comptonization consistently contributes a positive (hard) component to the time-lag (Miyamoto et al. 1988; Dutta & Chakrabarti 2016), whereas soft-lags are likely produced by the reflection of hard photons from the disc surface or by delays introduced through coronal outflows (Poutanen & Fabian 1999; Chatterjee et al. 2020).

Moreover, GRS 1915+105, a persistently variable and high-inclination source, has been shown to exhibit a transition from hard to soft-lags near ~ 2 Hz during plateau-state observations (Dutta et al. 2018), consistent with extensive *RXTE* studies of type-C QPOs (Zhang et al. 2020). At lower QPO frequencies (< 2 Hz), the source displays hard lags (Reig et al. 2000; Qu et al. 2010; Pahari et al. 2013; Dutta et al. 2018; Zhang et al. 2020). Interestingly, this characteristic lag sign reversal at ~ 2 Hz, commonly observed with *RXTE*, is absent in the *AstroSat* observations. Dutta & Chakrabarti (2016) explained that time lags can be positive across all energies in GRS 1915+105 as well as in XTE J1550–564 when the Comptonization efficiency exceeds $\sim 85\%$ in both sources. The lag switching at a specific frequency, recurring nearly 450 days later at a similar coronal size, suggests that coronal geometry plays a key role, with the net time lag determined by the relative contributions of the underlying physical processes. Nobili et al. (2000) considered a two-component thermal Comptonization scenario, where a hotter, optically thick inner corona up-scatters soft disc photons to higher energies, which are then down-scattered in a cooler, optically thin outer corona, producing soft-lags at high QPO frequencies (> 2 Hz). At lower QPO frequencies (< 2 Hz), the inner corona is assumed optically thin, producing only hard-lags. In this scenario, the inner disc radius is positively correlated

with the coronal size, whereas Karpouzas et al. (2021) reported an anti-correlation down to ~ 2 Hz, followed by a positive correlation at lower QPO frequencies. In GRS 1915+105, Méndez et al. (2022) explained that at QPO frequencies of 2–6 Hz, a hot and extended corona covering the inner disc enhances photon feedback onto the disc, producing soft lags interpreted as delayed disc responses to returning Comptonized photons. As the QPO frequency decreases, both lag amplitude and coronal size decrease while the disc recedes, near ~ 2 Hz, the lag approaches zero as the feedback fraction drops. At lower frequencies, the corona becomes vertically extended and may evolve into a jet-like structure, leading to positive lags despite weak feedback. However, these studies did not explain why lag switching is observed predominantly in high-inclination sources, while it is largely absent in low-inclination systems (Dutta & Chakrabarti 2016; van den Eijnden et al. 2017; Chatterjee et al. 2020; Choudhury et al. 2025). Moreover, the occurrence of a similar lag transition in GRS 1915+105 after ~ 450 days, at nearly the same QPO frequency, is unexpected given its highly turbulent accretion environment and complex variability, and its physical origin remains unexplained. Using *AstroSat* observations of MAXI J1535–571, Garg et al. (2022) suggested that low-frequency QPOs ($\nu_{\text{QPO}} < 2.2$ Hz) originate in the disc and propagate inward, whereas higher-frequency QPOs ($\nu_{\text{QPO}} > 2.2$ Hz) originate in the corona and propagate outward, resulting in net positive or negative lags depending on the dominant component.

Our spectro-temporal analysis (Fig. 6) shows that increasing fractional Comptonized flux (F_{Comp}) leads to progressively more positive time-lags, indicating that enhanced coronal Comptonization is responsible for hard-lag production. To probe the origin of the soft lags (1.59 – 13.49 ms) observed across all QPO frequencies in the *AstroSat* era without the sign reversal near ~ 2 Hz seen in *RXTE* data, we estimated the Comptonized flux (1 – 100 keV) using the model TBabs*(thcomp@diskbb). For $\nu_{\text{QPO}} < 2.2$ Hz, the Comptonized flux is significantly lower in *AstroSat* observations (ranges from $0.50 - 0.74 \times 10^{-8}$ erg.cm $^{-2}$.s $^{-1}$) than in *RXTE* (range from $1.56 - 3.08 \times 10^{-8}$ erg.cm $^{-2}$.s $^{-1}$), suggesting that the hard lags seen at ν_{QPO} during the *RXTE* era were driven by stronger Comptonization. Although both datasets show a similar correlation between time-lag and ν_{QPO} (see Fig. 4), the absence of a lag sign reversal in the *AstroSat* observations implies that comparable coronal geometries can yield different Comptonization strengths, resulting in either soft or hard lags. This behavior likely reflects variations in the coronal optical depth, particularly when additional processes such as enhanced reflection (Ross & Fabian 2007) or interactions with returning outflows (Patra et al. 2019; Chatterjee et al. 2020; Méndez et al. 2022) are weak or absent. Our previous study (Majumder et al. 2024) demonstrated that the optical depth of the Comptonizing medium plays a key role in producing hard or soft lags. Consistent with this, the soft lags observed at LFQPO frequencies in the present analysis, particularly during phases of lower Comptonized flux, are likely attributable to a higher coronal optical depth.

6 CONCLUSIONS

Understanding and interpreting the mechanisms behind the observed time-lags is challenging, as they arise from multiple non-linear and non-localized physical processes. In this work, we have correlated the spectral and temporal variability properties to investigate the time-lags associated with LFQPOs in persistently variable GRS 1915+105, using *AstroSat* observations from March 4, 2016 to March 22, 2019. A summary of our key findings is as follows,

- (i) LFQPOs are observed across four variability classes during

AstroSat observations: θ , β , ρ and χ where, χ class observations are further classified into χ_1 , χ_2 , χ_3 , and χ_4 based on their distinct spectro-temporal properties.

(ii) Class transitions occur within a few hours, either as a significant increase in X-ray photon count rate accompanied by a rise in QPO frequency, or vice versa, suggesting that fluctuations in the sub-Keplerian accretion rate likely drive the observed spectro-temporal evolution and trigger the variability class transitions.

(iii) The rms_{QPO} initially increases with QPO frequency up to ~ 3.4 Hz and then decreases at higher frequencies. A similar trend was seen in *RXTE* observations, though the maximum rms_{QPO} occurred at QPO frequency ~ 2 Hz.

(iv) The consistent increase of rms_{QPO} with F_{Comp} provides clear evidence that oscillations of the corona enhance the modulation of Comptonized photons, thereby increasing the rms power.

(v) Increasing F_{Comp} drives to higher rms_{QPO} and positive time-lag, while ν_{QPO} and Γ decrease, indicating that the time-lag arises from the combined effects of multiple mechanisms, i.e., Comptonization, reflection, outflows, and disc geometry.

(vi) The time-lag analysis reveals soft-lags (1.59–13.49 ms) across all QPO frequencies (1.38–7.38 Hz), with the soft-lag magnitude decreasing as ν_{QPO} increases, and without the sign reversal near ~ 2 Hz, observed in the *RXTE* data. The soft-lags observed at low LFQPO frequencies ($\nu_{\text{QPO}} < 2.2$ Hz) during phases of reduced Comptonized flux, compared to the *RXTE* era, are therefore likely attributable to a higher coronal optical depth.

ACKNOWLEDGEMENTS

We thank the anonymous reviewer for valuable suggestions and comments that helped to improve the quality of this manuscript. BGD, PM and AN acknowledge the support from ISRO sponsored project (DS-2B-1313(2)/6/2020-Sec.2). PM acknowledges the visit to Inter-University Centre for Astronomy and Astrophysics (IUCAA) where a partial amount of this work is carried out. PM also acknowledges the a short visit to Indian Institute of Astrophysics (IIA). BGD acknowledges ‘TARE’ scheme (Ref. No. TAR/2020/000141) under SERB, DST, Govt. of India and also acknowledges IUCAA for the Visiting Associate-ship Programme. AN thanks GH, SAG; DD, PDMSA, and Director, URSC for encouragement and continuous support to carry out this research. This work uses the data of *AstroSat* mission of ISRO which is archived at the Indian Space Science Data Centre (ISSDC). We have used the data of Soft X-ray Telescope (SXT) which is calibrated and verified by *AstroSat-SXT* team. We thank the SXT-POC team at TIFR for providing the necessary software tool to analyse SXT data. This work has also used *LAXPC* data which is verified by LAXPC-POC at TIFR. We thank *AstroSat* Science Support Cell for providing the software LAXPCsoftware for the analysis of *LAXPC* data.

DATA AVAILABILITY

Observational data of *RXTE* used for this work are available at the HEASARC website <https://heasarc.gsfc.nasa.gov/cgi-bin/W3Browse/w3browse.pl>. *AstroSat* archival data used for this work is available at the Astrobrowse (*AstroSat* archive) website https://webapps.issdc.gov.in/astro_archive/archive of the Indian Space Science Data Centre (ISSDC). The *MAXI/GSC* data is available in the website

<http://maxi.riken.jp/top/lc.html>. The *BAT* data is available in the website <https://swift.gsfc.nasa.gov/results/transients/>.

References

- Agrawal P. C., 2006, *Advances in Space Research*, **38**, 2989
- Agrawal V. K., Nandi A., Girish V., Ramadevi M. C., 2018, *MNRAS*, **477**, 5437
- Aktar R., Das S., Nandi A., Sreehari H., 2018, *Journal of Astrophysics and Astronomy*, **39**, 17
- Antia H. M., et al., 2017, *ApJS*, **231**, 10
- Antia H. M., et al., 2021, *Journal of Astrophysics and Astronomy*, **42**, 32
- Arnaud K. A., 1996, in Jacoby G. H., Barnes J., eds, *Astronomical Society of the Pacific Conference Series Vol. 101, Astronomical Data Analysis Software and Systems V*. p. 17
- Athulya M. P., Nandi A., 2023, *MNRAS*, **525**, 489
- Athulya M. P., Radhika D., Agrawal V. K., Ravishankar B. T., Naik S., Mandal S., Nandi A., 2022, *MNRAS*, **510**, 3019
- Banerjee A., Bhattacharjee A., Chatterjee D., Debnath D., Chakrabarti S. K., Katoch T., Antia H. M., 2021, *ApJ*, **916**, 68
- Belloni T., Hasinger G., 1990, *A&A*, **227**, L33
- Belloni T., Méndez M., King A. R., van der Klis M., van Paradijs J., 1997a, *ApJ*, **479**, L145
- Belloni T., Méndez M., King A. R., van der Klis M., van Paradijs J., 1997b, *ApJ*, **488**, L109
- Belloni T., Klein-Wolt M., Méndez M., van der Klis M., van Paradijs J., 2000, *A&A*, **355**, 271
- Belloni T. M., Sanna A., Méndez M., 2012, *MNRAS*, **426**, 1701
- Belloni T. M., Bhattacharya D., Caccese P., Bhalariao V., Vadawale S., Yadav J. S., 2019, *MNRAS*, **489**, 1037
- Belloni T. M., Méndez M., García F., Bhattacharya D., 2024, *MNRAS*, **527**, 7136
- Casella P., Belloni T., Homan J., Stella L., 2004, *A&A*, **426**, 587
- Casella P., Belloni T., Stella L., 2005, *ApJ*, **629**, 403
- Chakrabarti S. K., Manickam S. G., 2000, *ApJ*, **531**, L41
- Chakrabarti S. K., Nandi A., 2000, *arXiv e-prints*, pp astro-ph/0012526
- Chakrabarti S., Titarchuk L. G., 1995, *ApJ*, **455**, 623
- Chakrabarti S. K., Nandi A., Manickam S. G., Mandal S., Rao A. R., 2002, *ApJ*, **579**, L21
- Chakrabarti S. K., Nandi A., Choudhury A., Chatterjee U., 2004, *ApJ*, **607**, 406
- Chakrabarti S. K., Nandi A., Chatterjee A. K., Choudhury A. K., Chatterjee U., 2005, *A&A*, **431**, 825
- Chakrabarti S. K., Dutta B. G., Pal P. S., 2009, *MNRAS*, **394**, 1463
- Chatterjee A., Chakrabarti S. K., Ghosh H., 2017, *MNRAS*, **472**, 1842
- Chatterjee A., Dutta B. G., Nandi P., Chakrabarti S. K., 2020, *MNRAS*, **497**, 4222
- Chen X., Swank J. H., Taam R. E., 1997, *ApJ*, **477**, L41
- Choudhury S. D., Bhuvana G. R., Das S., Nandi A., 2025, *MNRAS*, **541**, 2934
- Cui W., 1999, *ApJ*, **524**, L59
- Das S., Chattopadhyay I., Nandi A., Molteni D., 2014, *MNRAS*, **442**, 251
- Das S., Nandi A., Agrawal V. K., Dihingia I. K., Majumder S., 2021, *MNRAS*, **507**, 2777
- Debnath D., Nath S. K., Chatterjee D., Chatterjee K., Chang H.-K., 2024, *ApJ*, **975**, 194
- Dutta B. G., Chakrabarti S. K., 2010, *MNRAS*, **404**, 2136
- Dutta B. G., Chakrabarti S. K., 2016, *ApJ*, **828**, 101
- Dutta B. G., Pal P. S., Chakrabarti S. K., 2018, *MNRAS*, **479**, 2183
- Ferreira J., et al., 2022, *A&A*, **660**, A66
- Frank J., King A., Raine D. J., 2002, *Accretion Power in Astrophysics: Third Edition*
- Garain S. K., Ghosh H., Chakrabarti S. K., 2014, *MNRAS*, **437**, 1329
- García F., Karpouzias K., Méndez M., Zhang L., Zhang Y., Belloni T., Altamirano D., 2022, *MNRAS*, **513**, 4196
- Garg A., Misra R., Sen S., 2022, *MNRAS*, **514**, 3285

- Harikesh S., Majumder S., Das S., Nandi A., 2025, *MNRAS*, **540**, 2965
- Huppenkothen D., Heil L. M., Hogg D. W., Mueller A., 2017, *MNRAS*, **466**, 2364
- Ingram A., Done C., Fragile P. C., 2009, *MNRAS*, **397**, L101
- Iyer N., Nandi A., Mandal S., 2015, *ApJ*, **807**, 108
- Kara E., Fabian A. C., Cackett E. M., Uttley P., Wilkins D. R., Zoghbi A., 2013, *MNRAS*, **434**, 1129
- Karpouzas K., Méndez M., García F., Zhang L., Altamirano D., Belloni T., Zhang Y., 2021, *MNRAS*, **503**, 5522
- Krimm H. A., et al., 2013, *ApJS*, **209**, 14
- Majumder S., Sreehari H., Aftab N., Katoch T., Das S., Nandi A., 2022, *MNRAS*, **512**, 2508
- Majumder P., Dutta B. G., Nandi A., 2024, *MNRAS*, **527**, 4739
- Majumder S., Das S., Nandi A., 2025a, *Publ. Astron. Soc. Australia*, **42**, e144
- Majumder P., Dutta B. G., Nandi A., 2025b, *MNRAS*, **540**, 37
- Makishima K., Maejima Y., Mitsuda K., Bradt H. V., Remillard R. A., Tuohy I. R., Hoshi R., Nakagawa M., 1986, *ApJ*, **308**, 635
- Markwardt C. B., Swank J. H., Taam R. E., 1999, *ApJ*, **513**, L37
- Méndez M., Karpouzas K., García F., Zhang L., Zhang Y., Belloni T. M., Altamirano D., 2022, *Nature Astronomy*, **6**, 577
- Mihara T., et al., 2011, *PASJ*, **63**, S623
- Misra R., Rawat D., Yadav J. S., Jain P., 2020, *ApJ*, **889**, L36
- Mitsuda K., et al., 1984, *PASJ*, **36**, 741
- Miyamoto S., Kitamoto S., Mitsuda K., Dotani T., 1988, *Nature*, **336**, 450
- Molteni D., Lanzafame G., Chakrabarti S. K., 1994, *ApJ*, **425**, 161
- Molteni D., Sponholz H., Chakrabarti S. K., 1996, *ApJ*, **457**, 805
- Motta S. E., et al., 2021, *MNRAS*, **503**, 152
- Muno M. P., Morgan E. H., Remillard R. A., 1999a, *ApJ*, **527**, 321
- Muno M. P., Morgan E. H., Remillard R. A., 1999b, *ApJ*, **527**, 321
- Nandi A., Manickam S. G., Rao A. R., Chakrabarti S. K., 2001a, *MNRAS*, **324**, 267
- Nandi A., Chakrabarti S. K., Vadawale S. V., Rao A. R., 2001b, *A&A*, **380**, 245
- Nandi A., Debnath D., Mandal S., Chakrabarti S. K., 2012, *A&A*, **542**, A56
- Nandi P., Chatterjee A., Chakrabarti S. K., Dutta B. G., 2021, *MNRAS*, **506**, 3111
- Nandi A., Das S., Majumder S., Katoch T., Antia H. M., Shah P., 2024, *MNRAS*, **531**, 1149
- Nobili L., Turolla R., Zampieri L., Belloni T., 2000, *ApJ*, **538**, L137
- Nowak M. A., Wilms J., Dove J. B., 1999, *ApJ*, **517**, 355
- Pahari M., Neilsen J., Yadav J. S., Misra R., Uttley P., 2013, *ApJ*, **778**, 136
- Patra D., Chatterjee A., Dutta B. G., Chakrabarti S. K., Nandi P., 2019, *ApJ*, **886**, 137
- Poutanen J., Fabian A. C., 1999, *MNRAS*, **306**, L31
- Qu J. L., Lu F. J., Lu Y., Song L. M., Zhang S., Ding G. Q., Wang J. M., 2010, *ApJ*, **710**, 836
- Radhika D., Nandi A., Agrawal V. K., Seetha S., 2016, *MNRAS*, **460**, 4403
- Rao A. R., Naik S., Vadawale S. V., Chakrabarti S. K., 2000, *A&A*, **360**, L25
- Rawat D., et al., 2019, *ApJ*, **870**, 4
- Reid M. J., McClintock J. E., Steiner J. F., Steeghs D., Remillard R. A., Dhawan V., Narayan R., 2014, *ApJ*, **796**, 2
- Reig P., Kylafis N. D., 2015, *A&A*, **584**, A109
- Reig P., Belloni T., van der Klis M., Méndez M., Kylafis N. D., Ford E. C., 2000, *ApJ*, **541**, 883
- Remillard R. A., McClintock J. E., 2006, *ARA&A*, **44**, 49
- Rodriguez J., Corbel S., Hannikainen D. C., Belloni T., Paizis A., Vilhu O., 2004, *ApJ*, **615**, 416
- Ross R. R., Fabian A. C., 2007, *MNRAS*, **381**, 1697
- Sahu P., Chand S., Thakur P., Dewangan G. C., Agrawal V. K., Tripathi P., Das S., 2024, *ApJ*, **975**, 165
- Seward F. D., Charles P. A., 2010, *Exploring the X-ray Universe*
- Singh K. P., et al., 2014, in Takahashi T., den Herder J.-W. A., Bautz M., eds, *Society of Photo-Optical Instrumentation Engineers (SPIE) Conference Series Vol. 9144, Space Telescopes and Instrumentation 2014: Ultraviolet to Gamma Ray*. p. 91441S, doi:10.1117/12.2062667
- Singh K. P., et al., 2017, *Journal of Astrophysics and Astronomy*, **38**, 29
- Soleri P., Belloni T., Casella P., 2008, *MNRAS*, **383**, 1089
- Sreehari H., Ravishankar B. T., Iyer N., Agrawal V. K., Katoch T. B., Mandal S., Nandi A., 2019, *MNRAS*, **487**, 928
- Sreehari H., Nandi A., Das S., Agrawal V. K., Mandal S., Ramadevi M. C., Katoch T., 2020, *MNRAS*, **499**, 5891
- Stella L., Vietri M., 1998, *ApJ*, **492**, L59
- Titarchuk L., Fiorito R., 2004, *ApJ*, **612**, 988
- Vadawale S. V., Rao A. R., Nandi A., Chakrabarti S. K., 2001a, *A&A*, **370**, L17
- Vadawale S. V., Rao A. R., Chakrabarti S. K., 2001b, *A&A*, **372**, 793
- Vadawale S. V., Rao A. R., Naik S., Yadav J. S., Ishwara-Chandra C. H., Pramesh Rao A., Pooley G. G., 2003, *ApJ*, **597**, 1023
- Vaughan B. A., Nowak M. A., 1997, *ApJ*, **474**, L43
- Wang X.-L., Yan Z., Xie F.-G., Wang J.-F., Ma R.-Y., 2024, *arXiv e-prints*, p. arXiv:2406.12477
- Wijnands R., Homan J., van der Klis M., 1999, *ApJ*, **526**, L33
- Wilms J., Allen A., McCray R., 2000, *ApJ*, **542**, 914
- Yadav J. S., et al., 2016, *ApJ*, **833**, 27
- Yadav J. S., Agrawal P. C., Antia H. M., Manchanda R. K., Paul B., Misra R., 2017, *Current Science*, **113**, 591
- Yan S.-P., Ding G.-Q., Wang N., Qu J.-L., Song L.-M., 2013, *MNRAS*, **434**, 59
- Zdziarski A. A., Johnson W. N., Magdziarz P., 1996, *MNRAS*, **283**, 193
- Zdziarski A. A., Szanecki M., Poutanen J., Gierliński M., Biernacki P., 2020, *MNRAS*, **492**, 5234
- Zhang L., et al., 2020, *MNRAS*, **494**, 1375
- van den Eijnden J., Ingram A., Uttley P., Motta S. E., Belloni T. M., Gardenier D. W., 2017, *MNRAS*, **464**, 2643
- van der Klis M., 1989, in Ögelman H., van den Heuvel E. P. J., eds, *NATO Advanced Study Institute (ASI) Series C Vol. 262, Timing Neutron Stars*. p. 27, doi:10.1007/978-94-009-2273-0_3
- van der Klis M., Hasinger G., Stella L., Langmeier A., van Paradijs J., Lewin W. H. G., 1987, *ApJ*, **319**, L13

This paper has been typeset from a $\text{\TeX}/\text{\LaTeX}$ file prepared by the author.